

Baryon Form Factors

Yong-Hui Lin^{a,b}, Hans-Werner Hammer^{b,c} and Ulf-G. Meißner^{a,d,e}

^aUniversität Bonn, Helmholtz Institut für Strahlen- und Kernphysik and Bethe Center for Theoretical Physics, 53115 Bonn, Germany

^bTechnische Universität Darmstadt, Department of Physics, 64289 Darmstadt, Germany

^cGSI Helmholtzzentrum für Schwerionenforschung GmbH, ExtreMe Matter Institute EMMI and Helmholtz Forschungsakademie Hessen für FAIR (HFHF), 64291 Darmstadt, Germany

^dForschungszentrum Jülich, Institute for Advanced Simulation (IAS-4), 52425 Jülich, Germany

^eBeihang University, Peng Huanwu Collaborative Center for Research and Education, Beijing 100191, China

© 20xx Elsevier Ltd. All rights reserved.

Chapter Article tagline: update of previous edition, reprint.

Contents

1	Introduction	1
2	Basics	2
2.1	Definitions	2
2.2	Experimental Observables	3
2.2.1	Space-like region	3
2.2.2	Time-like region	4
2.3	Spectral Decomposition and Dispersion Relations	4
3	Spectral Function and Constraints	5
3.1	Structure of the spectral functions	5
3.2	Constraints	7
4	Data Analysis and Uncertainties	8
5	Nucleon Form Factor Results	9
5.1	Spacelike Form Factors	10
5.2	Nucleon Radii	10
5.3	Timelike Form Factors	12
5.4	Remarks on the Pion Cloud	13
6	Hyperon form factors	14
7	Conclusions	14
	Acknowledgments	15
	References	15

Abstract

We review the status of baryon form factors with a special focus on the nucleon electromagnetic form factors which are known best. First, we give an introduction into the dispersive analyses and emphasize the role of unitarity and analyticity in the construction of the isoscalar and isovector spectral functions. Second, we present the state of the art in our understanding of nucleon form factors and radii including reliable uncertainty estimates from bootstrap and Bayesian methods. Third, we discuss the physics of the time-like form factors and point out further issues to be addressed in this framework. Finally, we review the status of hyperon form factors and comment on the pion cloud.

Keywords: nucleon structure, form factors, dispersion theory, nucleon radii, hyperon structure

1 Introduction

Baryons are composite particles made of three valence quarks bound together by the strong force. Understanding their structure and interactions is crucial for unraveling the complexities of quantum chromodynamics (QCD) [1, 2], the fundamental theory describing strong interactions in terms of quarks and gluons [3]. One of the key concepts for describing the internal structure of baryons and other strongly interacting particles (hadrons) are form factors. The form factors characterize how the response of composite objects to external probes differs from point particles. They describe the distribution of properties like charge, current, and spin within hadrons. Form factors are typically studied through scattering experiments, where a lepton interacts with a baryon via the exchange of a photon or a weak gauge boson. A theoretical discussion of the structure of baryons from the perspective of chiral perturbation theory and Schwinger-Dyson equations can, e.g., be found in Refs. [4] and [5], respectively.

In this chapter, we focus primarily on the electromagnetic (EM) form factors of the nucleon from the viewpoint of dispersion theory [6]. The nucleon (N) form factors are best understood experimentally and theoretically. They play a fundamental role since protons (p) and neutrons (n) essentially account for all the mass of everyday matter. The EM form factors of the nucleon describe the structure of the

nucleon as seen by an electromagnetic probe. As such, they provide a window on the strong interaction dynamics in the nucleon from large to small distances. At small momentum transfers, they probe the large-distance properties of the nucleon like the charge and magnetic moment, while the quark substructure of the nucleon determines the behavior at large momentum transfer. For recent reviews on the form factors see, e.g. Refs. [6–9]. The form factors enter in the description of a wide range of physical quantities ranging from the Lamb shift in atomic physics [10–13] over the strangeness content of the nucleon [14, 15] to the EM structure and reactions of atomic nuclei [16–18].

In contrast to the nucleon case, the experimental knowledge of the electromagnetic structure of other baryons and, in particular, of those with strangeness (the hyperons) is scarce due to absence of stable targets. So far, only the charge radius of the Σ^- , among all hyperons, has been measured to be 0.78(10) fm using a Σ^- beam at a mean energy of 610 GeV [19]. A new experimental approach to access the charge radii of charged hyperons was recently proposed by Ref. [20]. This technique extracts the low- t electromagnetic form factors in the unphysical region from the radiative Dalitz decay of charmonium, $\psi(2S) \rightarrow Y\bar{Y}e^+e^-$. The main source of information on Λ hyperon EM form factors in the time-like region are measurements of the reaction $e^+e^- \rightarrow \Lambda\bar{\Lambda}$ (see Ref. [21] for a review). A recent improvement of the data base for this reaction is provided by cross sections in the center-of-mass energy region from 3.51 to 4.6 GeV by the BESIII Collaboration [22], since previous measurements only covered the near-threshold region.

2 Basics

2.1 Definitions

The EM nucleon form factors and radii are determined by the matrix element of the electromagnetic current operator $j_\mu^{\text{EM}}(x)$ in the nucleon. Denoting a nucleon state with four-momentum p and spin s as $|N(p, s)\rangle$, this matrix element can be expressed as,

$$\langle N(p', s') | j_\mu^{\text{EM}}(0) | N(p, s) \rangle = \bar{u}(p', s') \left[F_1(t) \gamma_\mu + i \frac{F_2(t)}{2m} \sigma_{\mu\nu} q^\nu \right] u(p, s) \quad (1)$$

where m is the nucleon mass and $t = (p' - p)^2$ the four-momentum transfer squared. For space-like momentum transfer $t < 0$, it is convenient to use the variable $Q^2 = -t > 0$. The scalar functions $F_1(t)$ and $F_2(t)$ are the Dirac and Pauli form factors, respectively. Their normalization at $t = 0$ is determined by the charges and anomalous magnetic moments of the nucleon,

$$F_1^p(0) = 1, \quad F_1^n(0) = 0, \quad F_2^p(0) = \kappa_p, \quad F_2^n(0) = \kappa_n, \quad (2)$$

with $\kappa_p = 1.793$ and $\kappa_n = -1.913$ given in units of the nuclear magneton, $\mu_N = e/(2m)$. The magnetic moments of the proton and the neutron are thus given by $\mu_p = 1 + \kappa_p$ and $\mu_n = \kappa_n$, respectively.

For the dispersion-theoretical analysis, it is convenient to work in the isospin basis and to decompose the form factors into isoscalar (s) and isovector (v) parts,

$$F_i^s = \frac{1}{2}(F_i^p + F_i^n), \quad F_i^v = \frac{1}{2}(F_i^p - F_i^n), \quad i = 1, 2. \quad (3)$$

The experimental data are usually given in terms of the Sachs form factors,

$$G_E(t) = F_1(t) - \tau F_2(t), \quad G_M(t) = F_1(t) + F_2(t), \quad \text{where } \tau = -t/(4m^2), \quad (4)$$

because the differential cross sections have a simple dependence on the Sachs form factors (see below). Their definition, Eq. (4), implies that $G_E = G_M$ at the nucleon-antinucleon threshold, $t = 4m^2$. In the Breit frame, where the electromagnetic current transfers only three-momentum but no energy, the Sachs form factors G_E and G_M may be interpreted as the Fourier transforms of the charge and magnetization distributions, respectively. Note, however, that it has been repeatedly pointed out that the identification of spatial density distributions with the Fourier transform of the corresponding form factors in the Breit frame is problematic, see e.g. Refs. [23–25], and much work has been done to interpret the spatial density distributions of matrix elements of local operators [26–32].

The nucleon root mean square radii (loosely called radii), $r \equiv \sqrt{\langle r^2 \rangle}$, are defined via the expansion of the form factors around zero momentum transfer,

$$\frac{F(t)}{F(0)} = 1 + t \frac{\langle r^2 \rangle}{6} + \dots, \quad (5)$$

where $F(t)$ is a generic form factor. In the case of the electric and Dirac form factors of the neutron, G_E^n and F_1^n , the expansion starts with the term linear in t and the normalization factor $F(0)$ is dropped. In the space-like momentum transfer region, $t < 0$, the form factors are real valued quantities. In the time-like region, $t > 0$, the form factors are complex valued above the two-pion threshold at $t = 4M_\pi^2$ and thus throughout the physical region of the process $e^+e^- \rightarrow \bar{N}N$.

In Fig. 1, we sketch $G_E^p(t)$ and of $G_M^p(t)$ as examples. More precisely, the moduli of these form factors is depicted. For the space-like region, the physical threshold is located at $t = 0$, whereas the corresponding threshold in the time-like region is $t = 4m^2$. In between these two thresholds, the various vector meson poles (plus continua) build up the spectral function to be discussed in detail below. This region cannot be observed. We note that for the form factors in the time-like region, an additional complication arises due to the strong near-threshold nucleon-antinucleon interactions.

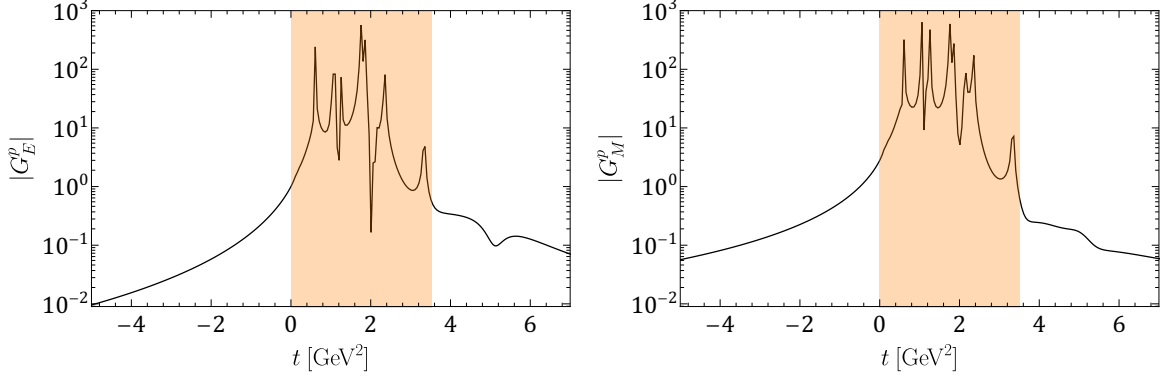


Fig. 1: The moduli of G_E^p (left panel) and G_M^p (right-panel) for space- and time-like momentum transfers based on a recent dispersion-theoretical analysis of form factor data [33]. The colored area between the two dashed lines at $t = 0$ and $t = 4m^2$ is the unphysical region where the form factor cannot be observed.

2.2 Experimental Observables

We start by discussing how the nucleon EM form factors can be accessed in experiment.

2.2.1 Space-like region

The space-like form factors (FFs) can be measured in elastic electron scattering. We consider for definiteness electron-proton (ep) scattering,

$$e(p_1) + p(p_2) \rightarrow e(p_3) + p(p_4), \quad (6)$$

where the four-momenta p_i are subject to the constraint $p_1 + p_2 = p_3 + p_4$. At first order in the EM fine-structure constant α , i.e. in the one-photon exchange approximation, the differential cross section can be expressed through the Sachs FFs as

$$\frac{d\sigma}{d\Omega} = \left(\frac{d\sigma}{d\Omega}\right)_{\text{Mott}} \frac{1}{\epsilon(1+\tau)} [\tau G_M^2(Q^2) + \epsilon G_E^2(Q^2)] = \left(\frac{d\sigma}{d\Omega}\right)_{\text{Mott}} \frac{\sigma_R}{\epsilon(1+\tau)}, \quad (7)$$

where $\epsilon = [1 + 2(1 + \tau) \tan^2(\theta/2)]^{-1}$ with $0 \leq \epsilon \leq 1$ is the virtual photon polarization, θ is the electron scattering angle in the laboratory frame, and $(d\sigma/d\Omega)_{\text{Mott}}$ is the Mott cross section. The latter corresponds to scattering off a point-like nucleon,

$$\left(\frac{d\sigma}{d\Omega}\right)_{\text{Mott}} = \frac{\alpha^2 \cos^2(\theta/2) E_3}{4E_1^2 \sin^4(\theta/2) E_1}, \quad (8)$$

where E_1 (E_3) is the energy of the incoming (outgoing) electron, related via $1/E_3 = 1/E_1 + (2/m) \sin^2(\theta/2)$. Two quantities out of the energies, momenta and angles suffice to determine this cross section and are related for such an elastic process. Specifically, in the laboratory frame with the initial nucleon at rest and neglecting the electron mass, we can write the four-momentum transfer

$$Q^2 \approx 4E_1 E_3 \sin^2(\theta/2). \quad (9)$$

In experiment, the differential cross section is usually given for a fixed total energy as a function of the scattering angle, so that a small scattering angle corresponds to a small momentum transfer. This is exactly the reason why a precise determination of the EM radii is so difficult. At large momentum transfer, the contribution from the magnetic form factor dominates the cross section. The contribution from the electric and the magnetic form factor can be read off from the reduced cross section σ_R defined in Eq. (7). The reduced cross section σ_R depends linearly on ϵ for a given Q^2 , with slope $G_E^2(Q^2)$ and intercept $\tau G_M^2(Q^2)$. This is called the Rosenbluth separation [34]. Two-photon corrections to this cross section need to be accounted when analyzing the real experimental data of the elastic electron-proton scattering, see Refs. [6, 35–38] for more details. Also, to investigate the neutron form factors, one measures electron scattering of a light nucleus like deuterium or ^3He . This requires, however, an accurate few-body calculation to disentangle the neutron FF contribution from the nuclear scattering cross section, as discussed briefly in Ref. [6].

In early ep scattering experiments, it was found that the form factors could be well approximated by the dipole form, $G_{\text{dip}}(Q^2)$,

$$G_E^p(Q^2) \simeq \frac{G_M^p(Q^2)}{\mu_p} \simeq \frac{G_M^n(Q^2)}{\mu_n} \simeq G_{\text{dip}}(Q^2) = (1 + Q^2/M_{\text{dip}}^2)^{-2}, \quad (10)$$

with $M_{\text{dip}}^2 = 0.71 \text{ GeV}^2$ the dipole mass. Moreover, $G_E^n(Q^2) = 0$ in this approximation. Employing these dipole FFs in the integrated cross section Eq. (7) defines the so-called dipole cross section, σ_{dip} . Often, the form factors or the measured cross sections are given relative to $G_{\text{dip}}(Q^2)$ and σ_{dip} , respectively.

A method to directly measure the form factor ratio G_E/G_M in polarized electron scattering off the proton, $\vec{e}p \rightarrow \vec{e}p$ (or similarly for scattering off the deuteron or ^3He), was proposed in Refs. [39, 40]. A simultaneous measurement of the two recoil polarizations

4 Baryon Form Factors

(longitudinal, P_l , and transverse, P_t) allows one to measure directly the ratio

$$R_p \equiv \mu_p \frac{G_E^p}{G_M^p} = -\mu_p \sqrt{\frac{\tau(1+\epsilon)}{2\epsilon}} \frac{P_t}{P_l}. \quad (11)$$

While this only determines the form factor ratio (and not the individual FFs), many systematic uncertainties cancel out and make this observable an important benchmark for any theoretical form factor calculation.

2.2.2 Time-like region

We now turn to the determination of the form factors in the time-like region. Here one needs a reaction in which a nucleon-antinucleon pair is produced electromagnetically. The FFs can, e.g., be extracted from the cross section data $e^+e^- \leftrightarrow \bar{p}p$ and $e^+e^- \rightarrow \bar{n}n$ for the proton and the neutron, respectively. As only very few differential cross section data exist in the time-like region, a separation of G_E and G_M is often not possible. One either makes an assumption like $G_E = G_M$ in the analysis of the data or one extracts the effective form factor $|G_{\text{eff}}|$, discussed below. For a review on the nucleon EM form factors in the time-like region, see Ref. [7]. Let us consider the process

$$e^+(p_1) + e^-(p_2) \rightarrow p(p_3) + \bar{p}(p_4), \quad (12)$$

in more detail. In the center-of-mass (CM) frame, we have $p_{1,2} = (E, \pm k_e)$ and $p_{3,4} = (E, \pm k_p)$. The photon momentum q then determines the center-of-mass energy by $q^2 = (p_1 + p_2)^2 = t = E_{\text{CM}}^2 = (2E)^2$. Time-like q implies positive q^2 in our metric. The three-momenta k_e and k_p enter in the phase-space factor $\beta = k_p/k_e$, which in the limit of neglecting the electron mass yields

$$\beta \approx k_p/E = \sqrt{1 - 4m_p^2/q^2}, \quad (13)$$

the velocity of the proton, and m_p is the proton mass. Denoting the emission angle of the proton by θ , the differential cross section in the one-photon-exchange approximation is

$$\frac{d\sigma}{d\Omega} = \frac{\alpha^2 \beta}{4q^2} C(q^2) \left[(1 + \cos^2 \theta) |G_M(q^2)|^2 + \frac{4m_p^2}{q^2} \sin^2 \theta |G_E(q^2)|^2 \right], \quad (14)$$

where $C(q^2)$ is the Sommerfeld-Gamow factor that accounts for the Coulomb interaction between the final-state particles

$$C(q^2) = \frac{y}{1 - e^{-y}}, \quad y = \frac{\pi \alpha m_p}{k_p}. \quad (15)$$

Integrating over the full angular distribution gives the total cross section

$$\sigma_{e^+e^- \rightarrow p\bar{p}}(q^2) = \frac{4\pi\alpha^2\beta}{3q^2} C(q^2) \left[|G_M(q^2)|^2 + \frac{2m_p^2}{q^2} |G_E(q^2)|^2 \right] \equiv \frac{4\pi\alpha^2\beta}{3q^2} C(q^2) \left(1 + \frac{2m_p^2}{q^2} \right) |G_{\text{eff}}^p(q^2)|^2. \quad (16)$$

which defines the effective form factor G_{eff} . For neutrons, the formulas are equivalent except for the Sommerfeld-Gamow factor which is not present in that case. Beyond the Coulomb final-state interactions, higher order QED corrections are usually neglected. For the time-reversed process, the phase space factor is inverted:

$$\sigma(e^+e^- \rightarrow p\bar{p}) = \beta^2 \sigma(p\bar{p} \rightarrow e^+e^-). \quad (17)$$

Polarization effects in $e^+e^- \rightarrow N\bar{N}$ are studied e.g. in Ref. [41].

2.3 Spectral Decomposition and Dispersion Relations

Dispersive methods provide a powerful tool to extract the form factors from experimental data. Dispersion relations (DRs) are based on unitarity and general analyticity properties of the form factors. Analog to the Kramers-Kronig relations from classical electrodynamics [42], they relate the real and imaginary parts of the form factors.

The imaginary part $\text{Im} F$ of a form factor F can be obtained from a spectral decomposition [43, 44]. For this purpose, we consider the electromagnetic current matrix element in the time-like region ($t > 0$), which is related to the space-like region ($t < 0$) via crossing symmetry. This matrix element is given by

$$J_\mu = \langle N(p_3) \bar{N}(p_4) | j_\mu^{\text{EM}}(0) | 0 \rangle = \bar{u}(p_3) \left[F_1(t) \gamma_\mu + i \frac{F_2(t)}{2m} \sigma_{\mu\nu} (p_3 + p_4)^\nu \right] v(p_4), \quad (18)$$

where p_3 and p_4 are the momenta of the nucleon and antinucleon created by the current j_μ^{EM} , respectively. For ease of notation, we have suppressed the corresponding spin indices. The four-momentum transfer squared in the time-like region is $t = (p_3 + p_4)^2$.

Using the LSZ reduction formalism, the imaginary part of the form factors is obtained by inserting a complete set of intermediate states [43, 44] as illustrated in Fig. 2,

$$\text{Im} J_\mu = \frac{\pi}{Z} (2\pi)^{3/2} \mathcal{N} \sum_n \langle N(p_3) | \bar{J}_N(0) | n \rangle \langle n | j_\mu^{\text{EM}}(0) | 0 \rangle v(p_4) \delta^{(4)}(p_3 + p_4 - p_n), \quad (19)$$

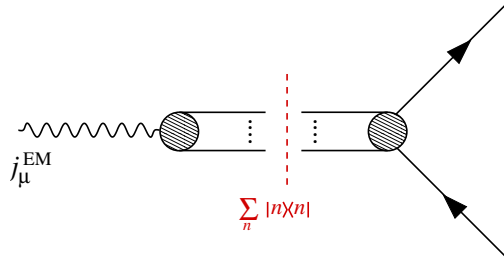


Fig. 2: Spectral decomposition of the matrix element of the electromagnetic current j_μ^{EM} in the nucleon. The intermediate states are denoted $|n\rangle$.

where N is a nucleon spinor normalization factor, Z is the nucleon wave function renormalization, and $\bar{J}_N(x) = J_N^\dagger(x)\gamma_0$ with $J_N(x)$ a nucleon source. It relates the spectral function to on-shell matrix elements of other processes, as detailed below.

The intermediate states $|n\rangle$ are asymptotic (observable) states of total four-momentum p_n . They carry the *same* quantum numbers as the current j_μ^{EM} :

$$\begin{aligned} I^G(J^{PC}) &= 0^-(1^{--}) && \text{for the isoscalar component ,} \\ I^G(J^{PC}) &= 1^+(1^{--}) && \text{for the isovector component ,} \end{aligned} \quad (20)$$

of the current j_μ^{EM} . Here, I and J denote the isospin $I = 0, 1$ and the angular momentum $J = 1$ of the photon, whereas G , P and C give the G -parity, parity and charge conjugation quantum number, respectively. Furthermore, these currents have zero net baryon number. Because of G -parity, states with an odd number of pions only contribute to the isoscalar part, while states with an even number contribute to the isovector part. For the isoscalar part the lowest mass states are:

$$3\pi, 5\pi, \dots, K\bar{K}, K\bar{K}\pi, \dots, \quad (21)$$

and for the isovector part they are:

$$2\pi, 4\pi, \dots, K\bar{K}, \dots \quad (22)$$

Associated with each intermediate state is a cut starting at the corresponding threshold in t and running to infinity. As a consequence, the spectral function $\text{Im} F(t)$ is different from zero along the cut from t_0 to ∞ , with $t_0 = 4$ (9) M_π^2 for the isovector (isoscalar) case.

The spectral functions are the central quantities in the dispersion-theoretical approach. Using Eqs. (18) and (19), they can in principle be obtained from experimental data. In practice, this program can only be carried out for the lightest two-particle intermediate states. The full structure of the spectral functions for the EM form factors of the nucleon is discussed in more detail below.

The typical singularity structure of a form factor F resulting from the spectral decomposition, Eq. (19), is shown in Fig. 3. We use Cauchy's theorem for F with the integration contour indicated in blue to obtain an unsubtracted dispersion relation of the form

$$F(t) = \frac{1}{\pi} \int_{t_0}^{\infty} \frac{\text{Im} F(t')}{t' - t - i\epsilon} dt', \quad (23)$$

where t_0 is the threshold of the lowest cut of $F(t)$ and the $i\epsilon$ defines the integral for values of t on the cut. The convergence of an unsubtracted dispersion relation for the form factors has been assumed. For proofs of such a representation in perturbation theory, see Ref. [45] (and references therein). One could also use a once-subtracted dispersion relation, since the normalization of the form factors at $t = 0$ is known. However, in what follows, we will only employ the unsubtracted form given in Eq. (23). For the parametrization of the spectral functions used below, the unsubtracted dispersion relations converge by construction. Consequently, by Eq. (23) the electromagnetic structure of the nucleon can be related to its absorptive behavior.

3 Spectral Function and Constraints

We continue to discuss the structure of the spectral function and constraints from theory and other processes.

3.1 Structure of the spectral functions

The longest-range and therefore at low momentum transfer most important continuum contribution comes from the 2π intermediate state which contributes to the isovector form factors [46]. A novel and very precise calculation of this contribution has recently been performed in Ref. [47] including the state-of-the-art pion-nucleon scattering amplitudes from dispersion theory. The resulting spectral functions exhibit the ρ -resonance at $\sqrt{t} = 0.77$ GeV as well as an enhancement on the left shoulder of the resonance. This confirms that the ρ is generated by unitarity [48] and no explicit ρ -meson is required in the isovector spectral function. The enhancement on the left shoulder of the ρ can be traced back to the fact that the partial wave amplitudes $f_{\pm}^1(t)$ have a singularity on the second Riemann sheet [49] (originating from the

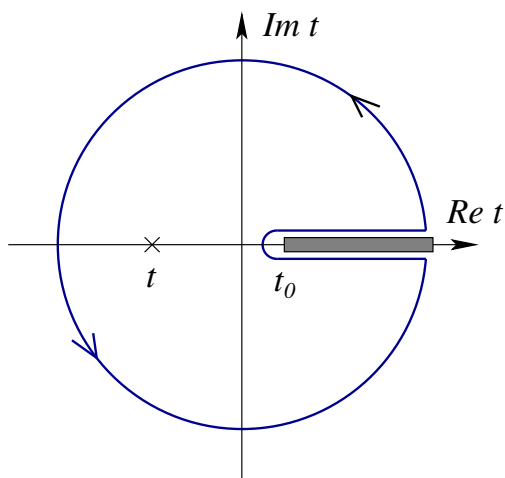


Fig. 3: Analytic structure of a typical form factor in the complex plane. The start of the lowest continuum cut is indicated by t_0 . The integration contour for the application of Cauchy's theorem to calculate the form factor $F(t)$ is shown in blue.

projection of the nucleon pole terms in the invariant pion-nucleon scattering amplitudes) located at

$$t_c = 4M_\pi^2 - \frac{M_\pi^4}{m^2} \approx 3.98 M_\pi^2, \quad (24)$$

very close to the physical threshold at $t_0 = 4M_\pi^2$.

Based on the DR, Eq. (23), it is straightforward to derive sum rules for the normalizations and radii of the isovector form factors. These were first considered in Ref. [46] for the various nucleon radii, see also [47],

$$\begin{aligned} \frac{1}{2}(r_E^v)^2 &= \frac{6}{\pi} \int_{4M_\pi^2}^{\infty} dt \frac{\text{Im} G_E^v(t)}{t^2} = \frac{1}{2} [(r_E^p)^2 - (r_E^n)^2], \\ \mu^v (r_M^v)^2 &= \frac{6}{\pi} \int_{4M_\pi^2}^{\infty} dt \frac{\text{Im} G_M^v(t)}{t^2} = \frac{1}{2} [(1 + \kappa_p)(r_M^p)^2 - \kappa_n (r_M^n)^2], \end{aligned} \quad (25)$$

where $\mu^v = (1 + \kappa_p - \kappa_n)/2 \approx 2.353$ is the isovector magnetic moment of the nucleon. Note that the sum rules for the radii remain unchanged if a once-subtracted dispersion relation is used instead of the unsubtracted one. Cutting the integrals off at $\Lambda = 2m$, one finds

$$\frac{1}{2}(r_E^v)^2 = 0.405(36) \text{ fm}^2 \quad \text{and} \quad \mu^v (r_M^v)^2 = 1.81(11) \text{ fm}^2. \quad (26)$$

It is remarkable that using a simple ρ -exchange with a Breit-Wigner or a Gounaris-Sakurai form [50], the corresponding isovector radii would be underestimated by about 40%. Thus, any dispersive analysis that does not include the full two-pion continuum but only the ρ -resonance in the isovector spectral function below 1 GeV will simply miss this important piece of physics.

The lowest isoscalar continuum is given by three-pion exchange. An analysis based on unitarity alone of this contribution does not exist, but it has been shown in chiral perturbation theory at leading [51] and subleading [52] orders, that there is no enhancement on the left wing of the ω resonance. Thus, in contrast to the ρ , the inclusion of the ω as a vector meson pole is justified. The first significant continuum contribution to the isoscalar spectral function is due to $K\bar{K}$ and $\rho\pi$ intermediate states. The contributions from the $K\bar{K}$ [53, 54] and $\rho\pi$ [55] were first included in the dispersive analysis of the EM form factors in Ref. [56]. For recent work on the isoscalar spectral functions in baryon chiral perturbation theory with explicit vector mesons, that strengthens the findings of these earlier works, see Ref. [57]. A more detailed discussion of these continua can be found in Ref. [6].

The remaining contributions to the spectral function can be parameterized by vector meson poles. On the one hand, the lower mass poles can be identified with physical vector mesons such as the ω and the ϕ . The higher mass poles on the other hand, are simply an effective way to parameterize higher mass strength in the spectral function. These effective poles at higher momentum transfers appear in both the isoscalar and isovector channels. Note that the contributions from the continua and the poles are sometimes strongly intertwined, e.g. the ρ -meson pole is indeed generated as part of the 2π -continuum, as known since long [48, 58, 59]. It should also be noted that we are dealing with an ill-posed problem [60, 61]. This implies that increasing the number of poles will from some point on not improve the description of the data. Therefore, the strategy has always been to use as few poles as possible. We come back to this issue in Sec. 4. The (isoscalar and

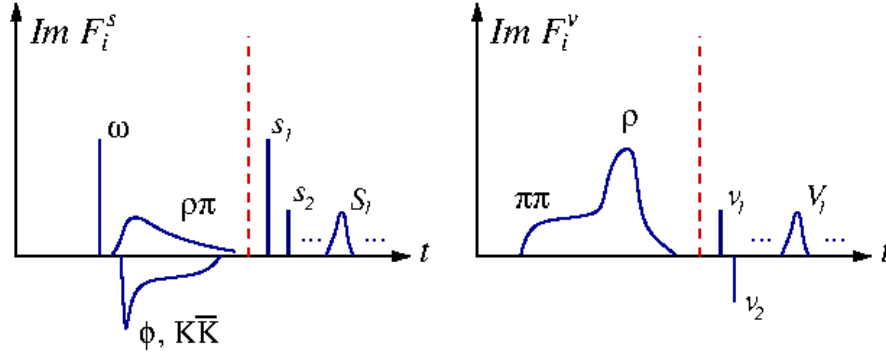


Fig. 4: Illustration of the isoscalar (left) and isovector (right) spectral function in terms of continua and (effective) vector meson poles. The vertical dashed line separates the well-constrained low-mass region from the high-mass region which is parameterized by narrow and broad effective poles, indicated by lower and upper case letters respectively.

isovector) spectral functions thus take the form

$$\text{Im } F_i^s(t) = \text{Im } F_i^{(s,K\bar{K})}(t) + \text{Im } F_i^{(s,\rho\pi)}(t) + \sum_{V=\omega,\phi,s_1,\dots} \pi a_i^V \delta(M_V^2 - t) + \sum_{V=S_1,\dots} \text{Im } F_i^{(s,V)}(t), \quad (27)$$

$$\text{Im } F_i^v(t) = \text{Im } F_i^{(v,2\pi)}(t) + \sum_{V=v_1,\dots} \pi a_i^V \delta(M_V^2 - t) + \sum_{V=V_1,\dots} \text{Im } F_i^{(v,V)}(t), \quad (28)$$

where $i = 1, 2$ and the broad effective poles are parameterized by a Breit-Wigner form. The masses of all effective poles and the widths of the broad poles are fitted to the data. Moreover, all vector meson coupling constants are fitted. A cartoon of these spectral functions is shown in Fig. 4. The vertical dashed line separates the phenomenologically well-constrained low-mass region from the effective vector meson poles at higher masses. Here, we allow a variable nonzero width for certain effective poles to mimic the imaginary part of the form factors in the higher- t time-like region, as was done in Ref. [56].

3.2 Constraints

The number of parameters in the spectral function (i.e. the various meson couplings a_i^V ($i = 1, 2$), the masses and widths of the effective poles) is reduced by enforcing various constraints.

The first set of constraints concerns the low- t behavior of the form factors. We enforce the correct normalization of the form factors as given in Eq. (2). The nucleon radii, however, are not included as a constraint. The exception to this is the squared neutron charge radius, which in some dispersive fits has been constrained to the value from low-energy neutron-atom scattering experiments [62, 63]. In the new fits discussed later, we implement this constraint using the high-precision determination of the neutron charge radius squared based on a chiral effective field theory analysis of electron-deuteron scattering [64, 65],

$$\langle r_n^2 \rangle = -0.105_{-0.006}^{+0.005} \text{ fm}^2. \quad (29)$$

Another set of constraints arises at large momentum transfers. Perturbative QCD (pQCD) constrains the behavior of the nucleon electromagnetic form factors for large momentum transfer. Brodsky and Lepage [66] worked out the behavior for $Q^2 \rightarrow \infty$,

$$F_i(t) \rightarrow \frac{1}{Q^{2(i+1)}} \left[\ln \left(\frac{Q^2}{\Lambda_{\text{QCD}}^2} \right) \right]^{-\gamma}, \quad i = 1, 2, \quad (30)$$

where $\gamma = 2 + 4/(3\beta)$ is an anomalous dimension and $\beta = 11 - 2N_f/3$ the leading order QCD β -function. The anomalous dimension $\gamma \approx 2$ depends weakly on the number of flavors, N_f [66]. The power behavior of the form factors at large Q^2 can be easily understood from perturbative gluon exchange. In order to distribute the momentum transfer from the virtual photon to all three quarks in the nucleon, at least two massless gluons have to be exchanged. Since each of the gluons has a propagator $\sim 1/Q^2$, the form factor has to fall off as $1/Q^4$. In the case of F_2 , there is additional suppression by $1/Q^2$ since a quark spin has to be flipped. The analytic continuation of the logarithm in Eq. (30) to time-like momentum transfers $-Q^2 \equiv t > 0$ yields an additional term, $\ln(-t/\Lambda^2) = \ln(t/\Lambda^2) - i\pi$ for $t > \Lambda^2$. The Phragmen-Lindelof theorem [49] therefore stipulates that the imaginary part has to vanish in the asymptotic limit. Taking these facts into account, the proton effective FF can be described for large time-like momentum transfer t by [67]

$$|G_{\text{eff}}^p(t)| = \frac{A}{t^2 (\ln^2(t/\Lambda^2) + \pi^2)}, \quad (31)$$

with the parameters from a fit to data prior to the 2013 measurement by the BaBar collaboration [68], given as $A = 72 \text{ GeV}^{-4}$ and $\Lambda = 0.52 \text{ GeV}$.

8 Baryon Form Factors

Enforcing the power law behavior of the form factors in the dispersion relation, Eq. (23), leads to superconvergence relations of the form

$$\int_{t_0}^{\infty} \text{Im} F_i(t) t^n dt = 0, \quad i = 1, 2, \quad (32)$$

with $n = 0$ for F_1 and $n = 0, 1$ for F_2 . These will be employed in the current analysis. In earlier DR analyses, modifications of the superconvergence relations were used including e.g. some higher order corrections. These should, however, be abandoned as the data are simply not sensitive to such corrections. We note that these superconvergence relations have already been used in Ref. [69], i.e. before the pQCD analysis [66].

Consequently, the number of effective poles is determined by the stability criterion mentioned before, that is, we take the minimum number of poles necessary to fit the data. The number of free parameters is then strongly reduced by the various constraints (unitarity, normalizations, superconvergence relations). These constraints can be implemented as what is called ‘‘hard constraints’’ or ‘‘soft constraints’’, respectively. In the former case, one solves a system of algebraic equations relating the various parameters (couplings, masses), thus reducing the number of free parameters in the fit (for an explicit representation, see e.g. [70]). In the latter case, the χ^2 is augmented by a Lagrange multiplier enforcing the corresponding constraints, see Sec. 4. Both options are viable and have been used.

It is straightforward to enumerate the number of fit parameters, which is given by the couplings and masses of the vector meson, $N_V = 4 + 3(N_S + N_V) + 4(N_S + N_V)$, with $N_{s/v}(N_{S/V})$ the number of the effective narrow (broad) isoscalar/isovector poles and the 4 represents the ω and ϕ couplings, minus the number of constraints, given by $N_C = 4 + 6 + 1$, referring to the low- t , the high- t constraints and the neutron charge radius squared, respectively. If the latter is not included, $N_C = 10$. Putting pieces together, we have in total $N_F = N_V - N_C = 3(N_S + N_V) + 4(N_S + N_V) - 7$ or $N_F = 3(N_S + N_V) + 4(N_S + N_V) - 6$ fit parameters (including or excluding the $(r_E^n)^2$ -constraint).

4 Data Analysis and Uncertainties

In this section, we briefly describe how the fits of the spectral functions to data are performed and how the statistical and systematic errors can be determined.

First, the quality of the fits is measured by means of two different χ^2 functions, χ_1^2 and χ_2^2 , which are defined as

$$\chi_1^2 = \sum_i \sum_k \frac{(n_k C_i - C(t_i, \theta_i, \mathbf{p}))^2}{(\sigma_i + \nu_i)^2}, \quad (33)$$

$$\chi_2^2 = \sum_{i,j} \sum_k (n_k C_i - C(t_i, \theta_i, \mathbf{p})) [V^{-1}]_{ij} (n_k C_j - C(t_j, \theta_j, \mathbf{p})), \quad (34)$$

where the C_i are the experimental data at the points t_i, θ_i and the $C(t_i, \theta_i, \mathbf{p})$ are the theoretical values for a given FF parametrization for the parameter values contained in \mathbf{p} . For total cross sections and form factor data the dependence on θ_i is dropped. Moreover, the n_k are normalization coefficients for the various data sets (labeled by the integer k and only used in the fits to the differential cross section data in the spacelike region), while σ_i and ν_i are their statistical and systematical errors, respectively. The covariance matrix $V_{ij} = \sigma_i \sigma_j \delta_{ij} + \nu_i \nu_j$. χ_2^2 is used for those experimental data where statistical and systematical errors are given separately, otherwise χ_1^2 is adopted. Furthermore, the χ^2 of each data set is normalized by the number of data points in order to weight the various data sets without bias.

One also considers the *reduced* χ^2 , which is given by:

$$\chi_{\text{red}}^2 = \frac{\chi_i^2}{N_D - N_F}, \quad i = 1, 2, \quad (35)$$

with N_D the number of fitted data points and N_F the number of independent fit parameters, see Sec. 3.2.

As noted in Sec. 3.2 the various constraints on the form factors can be implemented algebraically (hard constraints) or by modifying the χ^2 (soft constraints). The latter type of constraints are implemented as additive terms to the total χ^2 of the following form

$$\chi_{\text{add.}}^2 = p [x - \langle x \rangle]^2 \exp(p [x - \langle x \rangle]^2), \quad (36)$$

where $\langle x \rangle$ is the desired value and p is a strength parameter, which regulates the steepness of the exponential well and helps to stabilize the fits [56, 71]. The fits are performed with *MINUIT* [72] in Fortran.

We now turn to the estimation of uncertainty. One method to estimate the fit (statistical) errors is the bootstrap procedure, see e.g. Ref. [73]. One simulates a large number of data sets compared to the number of data points by randomly varying the points in the original set within the given errors assuming their normal distribution. Let us consider the radius extraction. In that case, one fits to each of these data sets separately, extracts the radius from each fit and consider the distribution of these radius values, which is sometimes denoted as bootstrap distribution. The artificial data sets represent many real samples. Therefore, this radius distribution emulates the probability distribution that one would get from fits to data from a high number of measurements. The precondition for using this method are independent and identically distributed data points. This is fulfilled when the χ^2 sum does not depend on the sequential order of the contributing points. For n simulated data sets, the errors thus scale with $1/\sqrt{n}$. However, to get a more realistic uncertainty, we exclude one percent of the data points from the sample and so can determine the lowest and highest value of the extracted radius. The same procedure can, of course, also be applied to the full form factors.

eff. poles	tot. χ^2	red. χ^2	r_E^p [fm]	r_M^p [fm]
$2s + 2v^*$	88.5046	1.321	0.829	0.843
$3s + 2v$	88.5159	1.383	0.829	0.861
$3s + 3v$	88.5051	1.451	0.828	0.848
$4s + 3v$	88.5037	1.526	0.829	0.843
$4s + 4v$	88.5046	1.609	0.829	0.845
$5s + 4v$	88.5027	1.702	0.829	0.837
$5s + 5v$	88.5043	1.806	0.828	0.861

Table 1: Fit to the PRad data with varying numbers of isoscalar (s) and isovector (v) effective poles. Given are the total and the reduced χ^2 and the resulting values for the proton radii. The * marks the best solution which defines the central values for the radii.

Another statistical tool to estimate the error intervals of our model parameters is the Bayesian approach, see e.g. Ref. [74] and references therein. In contrast to the interpretation of probabilities in the classical (also called frequentist) approach, where the probability is the frequency of an event to occur over a large number of repeated trials, the Bayesian method uses probabilities to express the current state of knowledge about the unknown parameters. This approach enables dynamic updates to parameter estimates, accounting for both the parameter value and its associated uncertainty in a unified probabilistic framework. The key ingredients to a Bayesian analysis are the prior distribution, which quantifies what is known about the model parameters prior to data being observed, and the likelihood function, which describes information about the parameters contained in the data. The prior distribution and likelihood can be combined to derive the posterior distribution by means of Bayes' theorem:

$$P(\text{paras}|\text{data}) = \frac{P(\text{paras})P(\text{data}|\text{paras})}{P(\text{data})}, \quad (37)$$

where “paras” denotes the parameters and $P(a|b)$ is the conditional probability that a happens given b .

It is the main goal of a Bayesian statistical analysis to obtain the posterior distribution of the model parameters. The posterior distribution contains the total knowledge about the model parameters after the data have been observed. From a Bayesian perspective, any statistical inference of interest can be obtained through an appropriate analysis of the posterior distribution. For example, point estimates of parameters are commonly computed as the mean of the posterior distribution and interval estimates can be calculated by producing the end points of an interval that correspond with specified percentiles of the posterior distribution. A powerful and easy-to-implement method to access the posterior distribution is the Markov Chain Monte Carlo (MCMC) algorithm. A systematic illustration of Bayesian analysis applications can be found in Ref. [75]. The analysis in [6] demonstrated that both bootstrap sampling and Bayesian simulation yield equivalent statistical errors for the form factors and radii. In the following, we will use the bootstrap procedure, as it is easier to implement for large data sets with a greater number of fit parameters.

Next, we discuss the extraction of the *systematic* uncertainties, which is always the most difficult task. Our strategy is similar to what was already done in Ref. [69], namely to vary the number of isoscalar and isovector poles around the values corresponding to the best solution, where the total χ^2 does not change by more than 1%. An example of this is given in Tab. 1 taken from Ref. [76] where only the PRad data [77] are considered. The best fit corresponds to 2 isoscalar and 2 isovector poles and the systematic errors in this case can be read off as [76]

$$\delta(r_E^p)_{\text{sys.}} = \pm 0.001 \text{ fm}, \quad \delta(r_M^p) = {}^{+0.018}_{-0.012} \text{ fm}. \quad (38)$$

While the absolute χ^2 does not change, the reduced one worsens as the number of fit parameter increases. As expected, the systematic error is larger for the magnetic radius as the electric FF dominates at low Q^2 .

5 Nucleon Form Factor Results

In this section, we present a variety of physics results based on a recent state-of-the-art dispersion theoretical analysis of the world data set [33]. Specifically, we discuss fits that include the differential cross section from the electron-proton elastic scattering, the proton FF ratio from the polarization transfer experiments and neutron FF data in the space-like region, as well as the effective FF for both the proton and neutron, and the proton FF ratio in the time-like region. The data base fitted in Ref. [33] is presented in Tab. 2. The best fit is found to consist of 3 narrow poles in the isoscalar channel (s) and 5 narrow poles in the isovector channel (v) below the nucleon-nucleon threshold and $3s + 3v$ broad poles above the threshold, that is, $N_s = 3$, $N_v = 5$ and $N_S = N_V = 3$. $\chi^2/\text{d.o.f} = 1.223$ is obtained for this best fit with the $(r_E^n)^2$ -constraint included. Note that there are 33 additional normalization constants for the MAMI and PRad data in the spacelike region. These are discussed in detail in Ref. [6]. We remark that fits with fixed normalizations lead to the same results but larger χ^2/dof . The vector meson parameters for the best fit can be found in the supplemental materials of Ref. [33].

Experimental data					
Region	Observables	Source	$ t $ GeV ²	number	References
spacelike $t < 0$	$d\sigma/d\Omega$	MAMI	0.00384-0.977	1422	[78]
		PRad	0.000215-0.058	71	[77]
	$\mu_p G_E^p/G_M^p$	JLab	1.18-8.49	16	[79–82]
	$\mu_n G_E^n/G_M^n$	world	1.58-3.41	4	[56]
	G_E^n	world	0.14-3.41	29	[56, 83]
	G_M^n	world	0.071-10.0	49	[56]
timelike $t > 0$	$ G_{\text{eff}}^p $	world	3.52-20.25	153	[68, 84–89]
	$ G_{\text{eff}}^n $	world	3.52-9.49	32	[90, 91]
	$ G_E^p/G_M^p $	BaBar	3.52-9.0	6	[84]
	$d\sigma/d\Omega$	BESIII	3.52-3.8	10	[68]

Table 2: Data base used in the dispersion-theoretical fits.

5.1 Spacelike Form Factors

In Fig. 5, we show our best fit compared to the experimental data for the ep cross section data from PRad (left upper panel) and MAMI (left lower panel), $\mu_p G_E^p/G_M^p$ from JLab (right top panel), the neutron electric form factor (right middle panel) and the neutron magnetic form factor (right bottom panel) at spacelike momentum transfer. Note that for the proton case, we fit to the ep cross section data with $Q^2 < 1$ GeV², incorporating with the proton form factor ratio data with $Q^2 > 1$ GeV². As in earlier fits [36, 76], the data for the proton form factor ratio $\mu_p G_E^p/G_M^p$ for $Q^2 < 1$ GeV², which do not participate in the fit, are well described, see the inset in the right top panel in Fig. 5. This points towards consistency between the two-photon corrected cross section data and the ratio data, that are not affected by such corrections.

Moreover, a decreasing behavior of $G_M^n/(\mu_n G_{\text{dip}})$ and $\mu_p G_E^p/G_M^p$ at large $|t|$ in the spacelike region is explicitly enforced in order to get a good description over the full range of momentum transfers. It turns out that a zero crossing of $\mu_p G_E^p/G_M^p$ is disfavored by the combined analysis of space- and timelike data, while some measurements suggest a zero crossing of this ratio around $t \approx -10$ GeV² [92]. Thus, data at higher momentum transfer than shown in the figure are required to settle this issue. We further remark that as in the earlier fits to the spacelike data only, the onset of perturbative QCD barely sets in at the highest momentum transfers probed.

Another facet of the spacelike FFs is the long-range part of the Breit-frame charge and magnetization distributions that follows from the Sachs form factors and can be interpreted in terms of a “pion cloud” and some additional short-range contributions from the ρ and other short-ranged physics. However, we emphasize that this separation is scale-dependent and thus not unique [93, 94]. We will come back to this issue in Sec. 5.4.

5.2 Nucleon Radii

Now, let us move to the nucleon radii. The radii extracted from the combined fits in [33] are

$$r_E^p = 0.840_{-0.002-0.002}^{+0.003+0.002} \text{ fm}, \quad r_M^p = 0.849_{-0.003-0.004}^{+0.003+0.001} \text{ fm}, \quad r_M^n = 0.864_{-0.004-0.001}^{+0.004+0.006} \text{ fm}, \quad (39)$$

where the first error is statistical (based on the bootstrap procedure) and the second one is systematic (based on the variations in the spectral functions). These values are in good agreement with previous high-precision analyses of spacelike data alone [6, 76] and have comparable errors.

Alternative information on the proton charge radius can be obtained from Lamb shift measurements in electronic as well as muonic hydrogen, see e.g. the reviews [95–97]. The proton radius puzzle—marked by a striking discrepancy between the proton charge radius extracted from muonic hydrogen spectroscopy [10, 98] and the value averaged from electron scattering and ordinary hydrogen spectroscopy [99] has driven extensive experimental efforts in elastic electron-proton scattering over the past decade.

For the proton charge radius r_E^p , we compare various dispersion-theoretical extractions from a historical perspective in Fig. 6. Note that here we only consider those dispersion-theoretical analyses that include the two-pion continuum explicitly in their spectral functions that is found to play a crucial role in the nucleon isovector form factors, see Refs. [6] for the details. It is remarkable that the dispersion-theoretical analyses always provided a consistent and robust proton charge radius in agreement with the spectroscopic values from muonic hydrogen [10, 98]. In Fig. 7, we list the most recent experimental determinations of the proton electric radius. Agreement on the proton charge radius has been achieved by the measurements from ep scattering, ep spectroscopy and the μp spectroscopy. As a consequence, the value collected in CODATA was updated in 2018 and the 2022 value is 0.84075(64) fm [100, 101] which agrees quite well with the dispersion theoretical determination of Ref. [33]. Moreover, the Zemach radius [102]

$$r_Z = -\frac{4}{\pi} \int_0^\infty \frac{dQ}{Q^2} \left[\frac{G_E(Q^2)G_M(Q^2)}{1+\kappa} - 1 \right], \quad (40)$$

and the third Zemach moment $\langle r^3 \rangle_{(2)}$, are obtained as

$$r_z = 1.054_{-0.002-0.001}^{+0.003+0.000} \text{ fm}, \quad \langle r^3 \rangle_{(2)} = 2.310_{-0.018-0.015}^{+0.022+0.014} \text{ fm}^3. \quad (41)$$

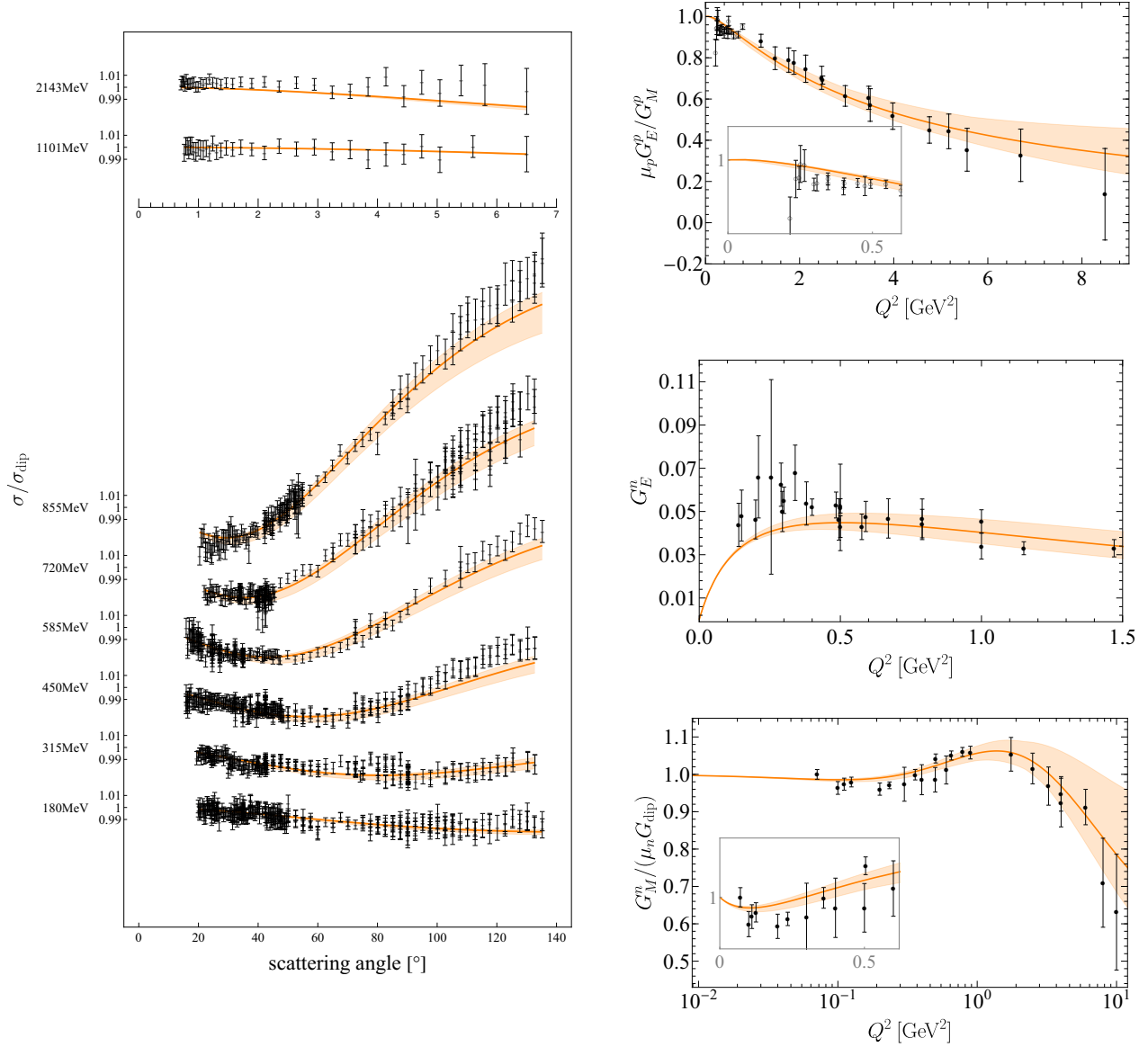


Fig. 5: Complete fit to space- and timelike data with bootstrap error (shaded band) compared to the ep cross section data from PRad (left upper panel) and MAMI (left lower panel), the JLab data for $\mu_p G_E^p / G_M^p$ (right top panel), the neutron electric form factor data (right middle panel) and the neutron magnetic form factor data (right bottom panel) at spacelike momentum transfer. Fitted data are depicted by closed symbols. The data for $|t| < 1 \text{ GeV}^2$ (open symbols, see also the inset) are shown for comparison only. The colored bands give the uncertainty due to the bootstrap procedure. Systematical uncertainties are not shown.

These values are in good agreement with Lamb shift and hyperfine splittings in muonic hydrogen [98].

While the electric radius of the proton has attracted much attention in the last decade, this is not true for its magnetic counterpart. The magnetic radius is not probed directly in the Lamb shift in electronic or muonic hydrogen and thus all existing information comes from electron scattering experiments. The ep cross section, however, is dominated by the electric form factor for small momentum transfer. Thus the magnetic radius r_M is more sensitive to larger momentum transfers, and it is not known experimentally with the same precision as r_E . The dispersion-theoretical values of the proton magnetic radius r_M^p were consistently bigger than 0.83 fm and slightly larger than r_E^p , as seen in Fig. 6. In stark contrast, the analysis of the A1 collaboration [103] yielded a significantly smaller value of $r_M = 0.777(13)_{\text{stat.}}(9)_{\text{syst.}}(5)_{\text{model}}(2)_{\text{group}}$ fm, including in addition to statistical and systematic uncertainties also some uncertainties from the fit model and differences between the two model groups used in the analysis. However, looking at the corresponding magnetic form factor $G_M(Q^2)$, it shows a pronounced bump-dip structure for momentum transfers $0 \leq Q^2 \leq 0.3 \text{ GeV}^2$. Such a structure is at odds with unitarity and analyticity [71, 94]. So is there other information available that could help to clarify this issue? Indeed, lattice QCD calculations at

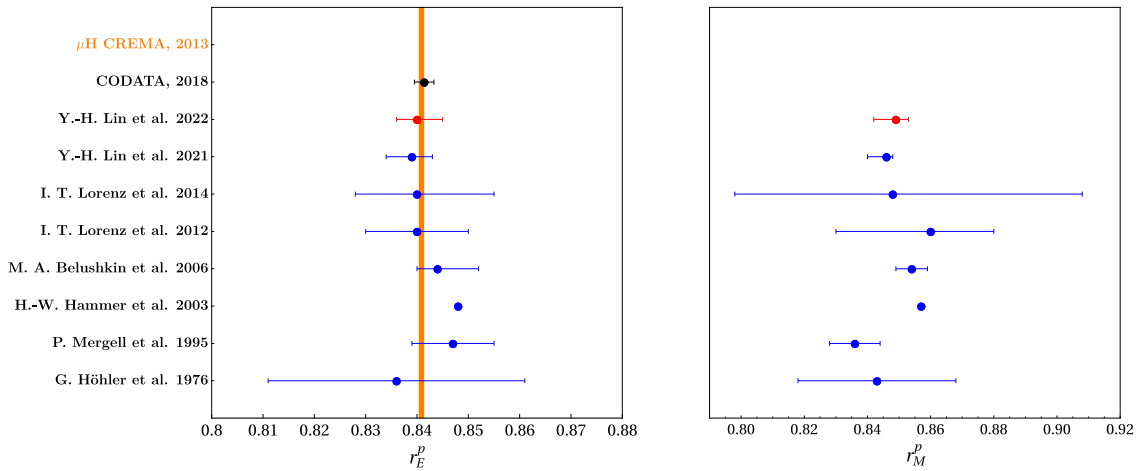


Fig. 6: Comparison of the proton electric (left) and magnetic (right) radii determined by various dispersion-theoretical extractions. The y-axis represents the date and first author of the corresponding work, see Ref. [6] for the relevant references. The orange band shows the latest radius extraction from the muonic hydrogen [98].

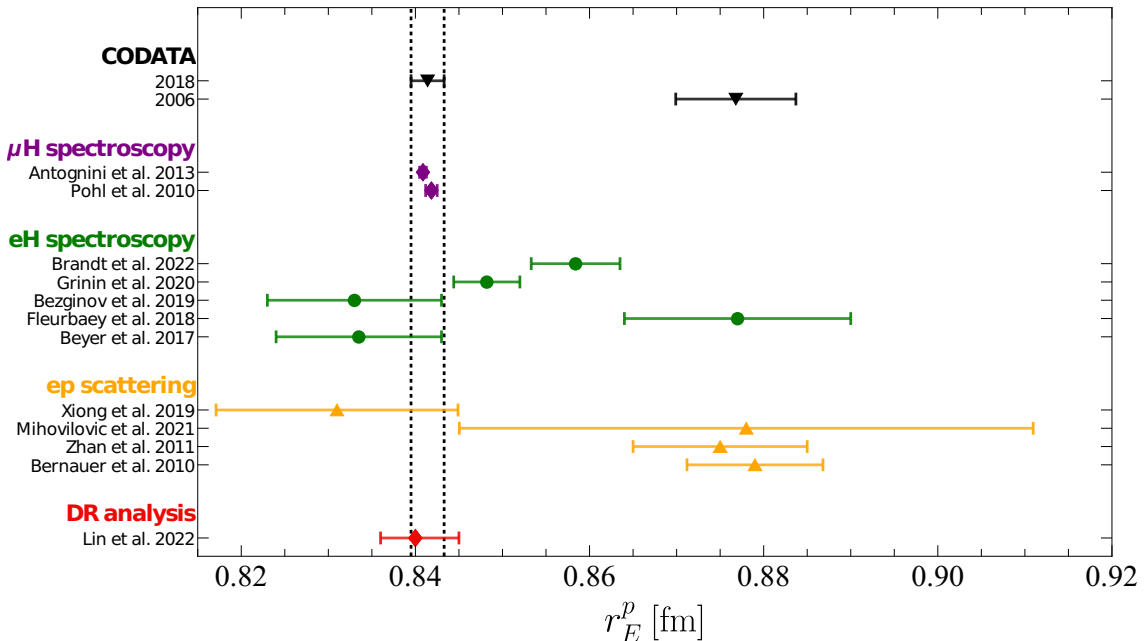


Fig. 7: Comparison of the proton charge radius extracted in Ref. [33] and other recent determinations. The y-axis indicates the process in which the proton charge radius was extracted as well as the date and first author of the corresponding work, see Ref. [6] for the relevant references.

physical pion masses are available. The latest lattice value for r_M given in Ref. [104], $r_M = 0.8111(89)$ fm, roughly corresponds to a 4σ deviation from the dispersive value. Note, however, that the electric radius in that work also comes out rather small, $r_E = 0.820(14)$ fm. The recent results by the PACS collaboration which include finite lattice spacing effects [105] also feature a small magnetic radius, but they have larger errors and are consistent with the dispersive value. These conflicting determinations of the proton magnetic radius appear to reveal a "new proton radius puzzle" [106]. Assuming that the proton electric radius is known now, a very precise determination of the Zemach radius, Eq. (40), which also enters into the Lamb shift, would give another independent determination of r_M that could help to clarify this issue.

5.3 Timelike Form Factors

In Fig. 8 and Fig. 9, we show our best fit compared to the experimental data for $|G_{\text{eff}}|$ of the proton and the neutron, respectively. We obtain a good description of the timelike data for $|G_{\text{eff}}|$. With $3s + 5v$ below-threshold narrow poles and $3s + 3v$ above-threshold broad poles, we

were able to reproduce both the visible near-threshold enhancement of the proton and the neutron timelike form factor (after subtraction of the electromagnetic final-state interaction in the proton case), first seen by the PS170 collaboration at LEAR [107], and the prominent oscillations in $|G_{\text{eff}}|$ between the threshold at $t = 4m^2$ and $t \approx 6 \text{ GeV}^2$. These poles also generate the imaginary part of the form factors in the physical region. Alternatively, these structures can also be generated by including contributions from triangle diagrams with $\Delta\bar{\Delta}$ and $(\Delta\bar{N} + \text{h.c.})$ intermediate states, see, e.g., Ref. [108]. In principle, these contributions are fixed. However, the corresponding coupling constants are poorly known and a perturbative treatment of these contributions is questionable. For further discussion, see Ref. [67]. Alternative interpretations of the oscillatory behavior of the timelike FFs of the nucleon are given in Refs. [109–112].

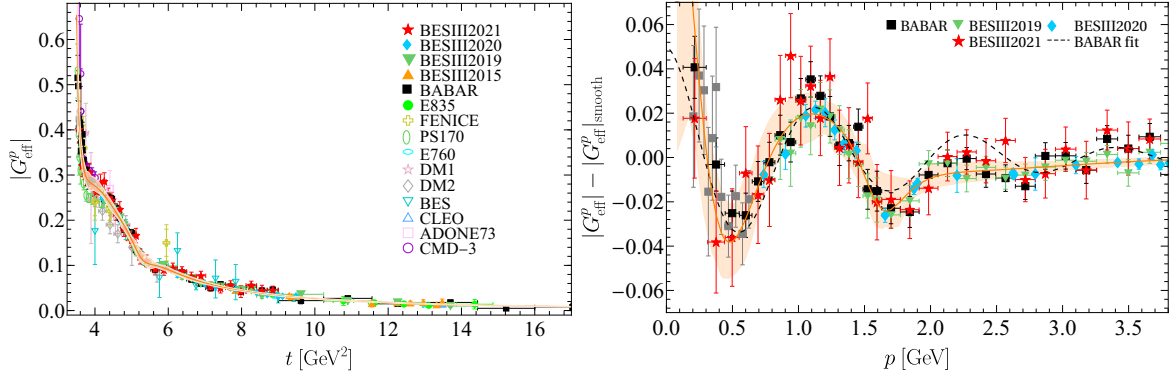


Fig. 8: Complete fit to space- and timelike data with bootstrap error (shaded band) compared to data for $|G_{\text{eff}}^p|$ of the proton (left panel) and the oscillatory behavior in detail (right panel). Fitted data are depicted by closed symbols; data given by open symbols are shown for comparison only (see Ref. [33] for explicit references). $|G_{\text{eff}}^p|_{\text{smooth}} = 7.7/(1 + t/14.8)/(1 - t/0.71)^2$ [68]. The black dashed line in the right plot show the phenomenological fit to BABAR data with the formula $F_p \equiv |G_{\text{eff}}^p| - |G_{\text{eff}}^p|_{\text{smooth}} = A \exp(-Bp) \cos(Cp + D)$ proposed in Ref. [67]. Here, p is the relative momentum of the proton.

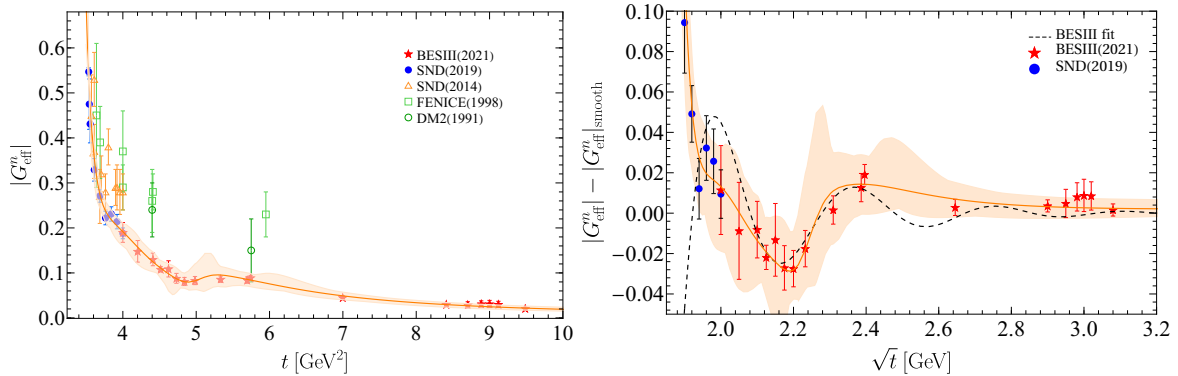


Fig. 9: Complete fit to space- and timelike data with bootstrap error (shaded band) compared to data for $|G_{\text{eff}}^n|$ of the neutron (left panel) and the oscillatory behavior in detail (right panel). Fitted data are depicted by closed symbols; data given by open symbols are shown for comparison only (see Ref. [33] for explicit references). $|G_{\text{eff}}^n|_{\text{smooth}} = 4.87/(1 + t/14.8)/(1 - t/0.71)^2$ [90]. The black dashed line in the right plot show the phenomenological fit to BESIII data with the formula [67] $F_n \equiv |G_{\text{eff}}^n| - |G_{\text{eff}}^n|_{\text{smooth}} = A \exp(-Bp) \cos(Cp + D)$, with p is the relative momentum of the neutron.

5.4 Remarks on the Pion Cloud

In the discussion of hadron properties the role of the pion cloud is frequently discussed. Long before the discovery of QCD, it was realized that pion-nucleon scattering data require a large coupling constant. As a consequence of this strong coupling, many virtual mesons – Yukawa’s pions – were expected to be associated with the nucleon, the pion cloud [113]. Many of these ideas have survived until today, but now we know that low-energy QCD is governed by the spontaneous breakdown of its chiral symmetry (for the light quarks) with the pion taking over a special role as a (Pseudo-)Goldstone boson. In this context, the pionic contribution to the nucleon (or more generally

baryon) structure, is called "pion cloud". While it is an important part of nucleon structure, in general it is not possible to uniquely and unambiguously define the contribution of the pion cloud to a given observable. An evaluation of the two-pion contribution to the nucleon electromagnetic form factors by use of dispersion relations and chiral perturbation theory to underline this point was given in Ref. [93].

Here we discuss the resolution dependence of the pion cloud in the framework of chiral perturbation theory (ChPT) [94]. To be precise, we consider a single nucleon. In baryon ChPT a nucleon typically emits a pion, this energetically forbidden πN intermediate state lives for a short while before the pion is reabsorbed by the nucleon, in accordance with the uncertainty principle. This mechanism generates the pion cloud of the nucleon, which in ChPT can be put on the firm ground of field theoretical principles. However, such loop contributions are in general scale-dependent, such that it is not possible to unambiguously define the pion cloud. As a consequence, the the concept of the pion cloud is resolution dependent.

To illustrate this fact, we consider the isovector Dirac radius of the proton as an example [114]. The first loop contributions appear at third order in the chiral expansion, leading to

$$\langle r^2 \rangle_1^v = \left[0.68 - (0.47 \text{ GeV}^2) \bar{d}(\mu) + 0.52 \ln(\mu/\text{GeV}) \right] \text{ fm}^2, \quad (42)$$

where $\bar{d}(\mu)$ is a pion-nucleon low-energy constant that parameterizes the nucleon core contribution. We emphasize that infinitely many combinations of $(\mu, \bar{d}(\mu))$ reproduce the empirical result $\langle r^2 \rangle_1^v = 0.585 \text{ fm}^2$ [56], e.g. $(1 \text{ GeV}, 0.20 \text{ GeV}^{-2})$, $(0.835 \text{ GeV}, 0.0 \text{ GeV}^{-2})$, and $(0.6 \text{ GeV}, -0.37 \text{ GeV}^{-2})$. Even the sign of the core contribution to the radius can change within a reasonable range typically used for the scale μ . Physical intuition tells us that the value for the coupling d should be negative such that the nucleon core gives a positive contribution to the isovector Dirac radius, but field theory shows that for (not unreasonable) regularization scales above $\mu = 835 \text{ MeV}$ this need not be the case. In essence, only the sum of the core and the cloud contribution constitutes a meaningful quantity that should be discussed. This observation holds for any observable - not just for the isovector Dirac radius discussed here. Consequently, an unambiguous extraction of the pion cloud contribution is not possible.

6 Hyperon form factors

The successful dispersive treatment of the nucleon EMFFs also holds much promise for a model-independent description of the electromagnetic structure of hyperon states. These form factors are much less well-known compared to the nucleon case and experimental data are only available in the timelike region [115], for a recent short review, see Ref. [116]. The authors of Ref. [117] considered once-subtracted dispersion relations for the electromagnetic Sigma-to-Lambda transition form factors and expressed these in terms of the pion EMFF and the two-pion-Sigma-Lambda scattering amplitudes. They predicted the electromagnetic Sigma-to-Lambda transition form factors and investigated the role of pion rescattering and the role of the explicit inclusion of the decuplet baryons in three-flavor chiral perturbation theory (ChPT). In [118], the dispersion theoretical determination of the electromagnetic Sigma-to-Lambda transition form factors was extended to include the $K\bar{K}$ intermediate state in $\pi\pi - K\bar{K}$ coupled-channel treatment in SU(3) ChPT. This resulted in a shift of the electric Sigma-to-Lambda transition form factor G_E , while the magnetic form factor G_M stays essentially unchanged. At present, the dispersion theoretical determination of electromagnetic Sigma-to-Lambda transition form factors suffers from sizeable uncertainties due to the poor knowledge of certain low-energy constants in SU(3) ChPT. The precise determination of this three-flavor LEC from the future experiments will be helpful to pin down the transition form factor. The electromagnetic form factors of the transition from the spin-3/2 Σ to the Λ hyperon were considered in Ref. [119]. Moreover, dispersion theory has been used to analyze the full set of cross section data for the reaction $e^+e^- \rightarrow \Lambda\bar{\Lambda}$ [120]. As more experimental data on the hyperon electromagnetic structure become available, dispersion theoretical methods provide a powerful tool to analyze these data and to predict space-like form factors from experimental data in the time-like region. They also provide valuable insights in the underlying mechanisms.

7 Conclusions

This chapter reviews the status of baryon form factors with a special focus on the nucleon EM form factors which are known best. In particular, we discuss the dispersion-theoretical approach to the nucleon EM form factors as well as radii and highlight recent progress in the field. We emphasize that this approach has matured and become a precision tool to analyze electron scattering and form factor ratio data. We stress that DRs have consistently found a small proton charge radius, $r_E^p \simeq 0.84 \text{ fm}$, with a slightly larger proton magnetic radius, $r_M^p \simeq 0.85 \text{ fm}$. Regarding the latter, we point out that there are a number of conflicting determinations, which could be regarded as a new "proton radius puzzle". We have also discuss our present understanding of the physics in both the space- and time-like regions. Firstly, the combined analysis of space- and timelike data disfavors a zero crossing for the proton FF ratio $\mu_p G_E^p / G_M^p$ at spacelike momentum transfer. Secondly, both the strong near-threshold enhancement and the prominent oscillations in $|G_{\text{eff}}|$ between the threshold at $t = 4m^2$ and $t \approx 6 \text{ GeV}^2$ can be described after introducing a certain number of broad poles above threshold in the spectral functions. These poles also generate the imaginary part of the form factors in the physical region. Finally, we review the status of hyperon form factors and comment on the scale-dependence of the pion cloud.

We close with some open questions related to baryon form factors that require more data and/or further investigations:

- For the neutron data basis, a thorough analysis of the existing electron-deuteron and electron-³He scattering data based on chiral effective field theory and including two-photon corrections should be performed. This would allow to consistently analyze the proton and neutron form factors based on the dispersive approach applied directly to cross section data.
- Data on ep scattering or the polarization transfer at $Q^2 \gg 10 \text{ GeV}^2$ are urgently needed to investigate the onset of perturbative QCD. It will also be interesting to find out whether the form factor ratio really crosses zero as the present data seem to indicate.
- The precise experimental determination of the proton magnetic radius is urgently required to figure out whether a new "proton radius puzzle" exists.
- The current dispersion theoretical analysis of the nucleon electromagnetic form factor need to be expanded to incorporate the upcoming muon-proton scattering data from the MUSE [121] and AMBER [122], aiming to definitively resolve the proton radius.
- In the case of the hyperon form factors, the data basis in the timelike region is slowly increasing, mostly through measurements from the BESIII collaboration. Here, the interplay of final-state interactions in the proton-antiproton system and of genuine resonance contributions is an important ingredient, but at present the main unresolved problems and challenges reside on the experimental side. In particular, more differential cross section data are urgently required.

Acknowledgments

The work of UGM and YHL was supported in part by the Deutsche Forschungsgemeinschaft (DFG, German Research Foundation) and the NSFC through the funds provided to the Sino-German Collaborative Research Center TRR 110 "Symmetries and the Emergence of Structure in QCD" (DFG Project-ID 196253076 - TRR 110, NSFC Grant No. 12070131001), by the Chinese Academy of Sciences (CAS) through a President's International Fellowship Initiative (PIFI) (Grant No. 2025PD0022), and by the EU Horizon 2020 research and innovation programme, STRONG-2020 project under grant agreement No. 824093. UGM was also supported by the ERC AdG EXOTIC (grant No. 101018170) by the MKW NRW under the funding code No. NW21-024-A. HWH was supported by the Deutsche Forschungsgemeinschaft (DFG, German Research Foundation) – Projektnummer 279384907 – CRC 1245 and by the German Federal Ministry of Education and Research (BMBF) (Grants No. 05P21RDFNB and 05P24RDB).

References

- [1] Kenneth G. Wilson, Confinement of Quarks, *Phys. Rev. D* 10 (1974) 2445–2459, doi:10.1103/PhysRevD.10.2445.
- [2] Frank Wilczek, Origins of Mass, *Central Eur. J. Phys.* 10 (2012) 1021–1037, doi:10.2478/s11534-012-0121-0, 1206.7114.
- [3] Franz Gross, et al., 50 Years of Quantum Chromodynamics, *Eur. Phys. J. C* 83 (2023) 1125, doi:10.1140/epjc/s10052-023-11949-2, 2212.11107.
- [4] Bastian Kubis, Ulf-G. Meißner, Baryon form-factors in chiral perturbation theory, *Eur. Phys. J. C* 18 (2001) 747–756, doi:10.1007/s100520100570, hep-ph/0010283.
- [5] Gernot Eichmann, Helios Sanchis-Alepuz, Richard Williams, Reinhard Alkofer, Christian S. Fischer, Baryons as relativistic three-quark bound states, *Prog. Part. Nucl. Phys.* 91 (2016) 1–100, doi:10.1016/j.pnpnp.2016.07.001, 1606.09602.
- [6] Yong-Hui Lin, Hans-Werner Hammer, Ulf-G. Meißner, Dispersion-theoretical analysis of the electromagnetic form factors of the nucleon: Past, present and future, *Eur. Phys. J. A* 57 (8) (2021) 255, doi:10.1140/epja/s10050-021-00562-0, 2106.06357.
- [7] Achim Denig, Giovanni Salme, Nucleon Electromagnetic Form Factors in the Timelike Region, *Prog. Part. Nucl. Phys.* 68 (2013) 113–157, doi:10.1016/j.pnpnp.2012.09.005, 1210.4689.
- [8] S. Pacetti, R. Baldini Ferroli, E. Tomasi-Gustafsson, Proton electromagnetic form factors: Basic notions, present achievements and future perspectives, *Phys. Rept.* 550-551 (2015) 1–103, doi:10.1016/j.physrep.2014.09.005.
- [9] V. Punjabi, C. F. Perdrisat, M. K. Jones, E. J. Brash, C. E. Carlson, The Structure of the Nucleon: Elastic Electromagnetic Form Factors, *Eur. Phys. J. A* 51 (2015) 79, doi:10.1140/epja/i2015-15079-x, 1503.01452.
- [10] Randolf Pohl, et al., The size of the proton, *Nature* 466 (2010) 213–216, doi:10.1038/nature09250.
- [11] Axel Beyer, et al., The Rydberg constant and proton size from atomic hydrogen, *Science* 358 (6359) (2017) 79–85, doi:10.1126/science.aah6677.
- [12] H el ene Fleurbaey, Sandrine Galtier, Simon Thomas, Marie Bonnaud, Lucile Julien, Fran ois Biraben, Fran ois Nez, Michel Abgrall, Jocelyne Gu ena, New Measurement of the $1S - 3S$ Transition Frequency of Hydrogen: Contribution to the Proton Charge Radius Puzzle, *Phys. Rev. Lett.* 120 (18) (2018) 183001, doi:10.1103/PhysRevLett.120.183001, 1801.08816.
- [13] N. Bezginov, T. Valdez, M. Horbatsch, A. Marsman, A. C. Vutha, E. A. Hessels, A measurement of the atomic hydrogen Lamb shift and the proton charge radius, *Science* 365 (6457) (2019) 1007–1012, doi:10.1126/science.aau7807.
- [14] D. S. Armstrong, R. D. McKeown, Parity-Violating Electron Scattering and the Electric and Magnetic Strange Form Factors of the Nucleon, *Ann. Rev. Nucl. Part. Sci.* 62 (2012) 337–359, doi:10.1146/annurev-nucl-102010-130419, 1207.5238.
- [15] F. E. Maas, K. D. Paschke, Strange nucleon form-factors, *Prog. Part. Nucl. Phys.* 95 (2017) 209–244, doi:10.1016/j.pnpnp.2016.11.001.
- [16] Sonia Bacca, Saori Pastore, Electromagnetic reactions on light nuclei, *J. Phys. G* 41 (12) (2014) 123002, doi:10.1088/0954-3899/41/12/123002, 1407.3490.
- [17] Daniel R. Phillips, Electromagnetic Structure of Two- and Three-Nucleon Systems: An Effective Field Theory Description, *Ann. Rev. Nucl. Part. Sci.* 66 (2016) 421–447, doi:10.1146/annurev-nucl-102014-022321.
- [18] Hermann Krebs, Nuclear Currents in Chiral Effective Field Theory, *Eur. Phys. J. A* 56 (9) (2020) 234, doi:10.1140/epja/s10050-020-00230-9, 2008.00974.
- [19] Ivo M. Gough Eschrich, et al. (SELEX), Measurement of the Sigma- Charge Radius by Sigma- Electron Elastic Scattering, *Phys. Lett. B* 522 (2001) 233–239, doi:10.1016/S0370-2693(01)01285-0, hep-ex/0106053.
- [20] Yong-Hui Lin, Feng-Kun Guo, Ulf-G. Meißner, Method for measuring the charge radii of charged hyperons from the time-like region, *Phys. Lett. B* 856 (2024) 138887, doi:10.1016/j.physletb.2024.138887, 2309.07850.

- [21] Xiaorong Zhou, Liang Yan, Rinaldo Baldini Ferroli, Guangshun Huang, Experimental Review of $\Lambda\bar{\Lambda}$ Production, *Symmetry* 14 (1) (2022) 144, doi:10.3390/sym14010144.
- [22] M. Ablikim, et al. (BESIII), Measurement of the cross section for $e^+e^- \rightarrow \Lambda\bar{\Lambda}$ and evidence of the decay $\psi(3770) \rightarrow \Lambda\bar{\Lambda}$, *Phys. Rev. D* 104 (9) (2021) L091104, doi:10.1103/PhysRevD.104.L091104, 2108.02410.
- [23] Matthias Burkardt, Impact parameter dependent parton distributions and off forward parton distributions for zeta $\rightarrow 0$, *Phys. Rev. D* 62 (2000) 071503, doi:10.1103/PhysRevD.62.071503, [Erratum: *Phys.Rev.D* 66, 119903 (2002)], hep-ph/0005108.
- [24] Gerald A. Miller, Charge Density of the Neutron, *Phys. Rev. Lett.* 99 (2007) 112001, doi:10.1103/PhysRevLett.99.112001, 0705.2409.
- [25] Robert L. Jaffe, Ambiguities in the definition of local spatial densities in light hadrons, *Phys. Rev. D* 103 (1) (2021) 016017, doi:10.1103/PhysRevD.103.016017, 2010.15887.
- [26] Gerald A. Miller, Transverse Charge Densities, *Ann. Rev. Nucl. Part. Sci.* 60 (2010) 1–25, doi:10.1146/annurev.nucl.012809.104508, 1002.0355.
- [27] Yuxun Guo, Xiangdong Ji, Kyle Shiells, Novel twist-three transverse-spin sum rule for the proton and related generalized parton distributions, *Nucl. Phys. B* 969 (2021) 115440, doi:10.1016/j.nuclphysb.2021.115440, 2101.05243.
- [28] Julia Yu. Panteleeva, Maxim V. Polyakov, Forces inside the nucleon on the light front from 3D Breit frame force distributions: Abel tomography case, *Phys. Rev. D* 104 (1) (2021) 014008, doi:10.1103/PhysRevD.104.014008, 2102.10902.
- [29] Cédric Lorcé, Hervé Moutarde, Arkadiusz P. Trawiński, Revisiting the mechanical properties of the nucleon, *Eur. Phys. J. C* 79 (1) (2019) 89, doi:10.1140/epjc/s10052-019-6572-3, 1810.09837.
- [30] Adam Freese, Gerald A. Miller, Forces within hadrons on the light front, *Phys. Rev. D* 103 (2021) 094023, doi:10.1103/PhysRevD.103.094023, 2102.01683.
- [31] E. Epelbaum, J. Gegelia, N. Lange, U.-G. Meißner, M. V. Polyakov, Definition of Local Spatial Densities in Hadrons, *Phys. Rev. Lett.* 129 (1) (2022) 012001, doi:10.1103/PhysRevLett.129.012001, 2201.02565.
- [32] J. Yu. Panteleeva, E. Epelbaum, J. Gegelia, U.-G. Meißner, Definition of electromagnetic local spatial densities for composite spin-1/2 systems, *Phys. Rev. D* 106 (5) (2022) 056019, doi:10.1103/PhysRevD.106.056019, 2205.15061.
- [33] Yong-Hui Lin, Hans-Werner Hammer, Ulf-G. Meißner, New Insights into the Nucleon’s Electromagnetic Structure, *Phys. Rev. Lett.* 128 (5) (2022) 052002, doi:10.1103/PhysRevLett.128.052002, 2109.12961.
- [34] M. N. Rosenbluth, High Energy Elastic Scattering of Electrons on Protons, *Phys. Rev.* 79 (1950) 615–619, doi:10.1103/PhysRev.79.615.
- [35] J. Arrington, P. G. Blunden, W. Melnitchouk, Review of two-photon exchange in electron scattering, *Prog. Part. Nucl. Phys.* 66 (2011) 782–833, doi:10.1016/j.pnpnp.2011.07.003, 1105.0951.
- [36] I. T. Lorenz, Ulf-G. Meißner, H.-W. Hammer, Y. B. Dong, Theoretical Constraints and Systematic Effects in the Determination of the Proton Form Factors, *Phys. Rev. D* 91 (1) (2015) 014023, doi:10.1103/PhysRevD.91.014023, 1411.1704.
- [37] A. Afanasev, P. G. Blunden, D. Hasell, B. A. Raue, Two-photon exchange in elastic electron–proton scattering, *Prog. Part. Nucl. Phys.* 95 (2017) 245–278, doi:10.1016/j.pnpnp.2017.03.004, 1703.03874.
- [38] Jaseer Ahmed, P. G. Blunden, W. Melnitchouk, Two-photon exchange from intermediate state resonances in elastic electron–proton scattering, *Phys. Rev. C* 102 (4) (2020) 045205, doi:10.1103/PhysRevC.102.045205, 2006.12543.
- [39] A. I. Akhiezer, Mikhail. P. Rekalo, Polarization phenomena in electron scattering by protons in the high energy region, *Sov. Phys. Dokl.* 13 (1968) 572.
- [40] R. G. Arnold, Carl E. Carlson, Franz Gross, Polarization Transfer in Elastic electron Scattering from Nucleons and Deuterons, *Phys. Rev. C* 23 (1981) 363, doi:10.1103/PhysRevC.23.363.
- [41] A. Z. Dubnickova, S. Dubnicka, M. P. Rekalo, Investigation of the nucleon electromagnetic structure by polarization effects in $e^+e^- \rightarrow N$ anti- N processes, *Nuovo Cim. A* 109 (1996) 241–256, doi:10.1007/BF02731012.
- [42] John David Jackson, *Classical Electrodynamics*, Wiley 1998.
- [43] Geoffrey F. Chew, Robert Karplus, Stephen Gasiorowicz, Fredrik Zachariasen, Electromagnetic Structure of the Nucleon in Local-Field Theory, *Phys. Rev.* 110 (1) (1958) 265, doi:10.1103/PhysRev.110.265.
- [44] P. Federbush, M. L. Goldberger, S. B. Treiman, Electromagnetic Structure of the Nucleon, *Phys. Rev.* 112 (1958) 642–665, doi:10.1103/PhysRev.112.642.
- [45] S.D. Drell, F. Zachariasen, *Electromagnetic Structure of Nucleons*, Oxford University Press 1961.
- [46] G. Höhler, E. Pietarinen, Electromagnetic Radii of Nucleon and Pion, *Phys. Lett. B* 53 (1975) 471–475, doi:10.1016/0370-2693(75)90220-8.
- [47] M. Hoferichter, B. Kubis, J. Ruiz de Elvira, H.-W. Hammer, U.-G. Meißner, On the $\pi\pi$ continuum in the nucleon form factors and the proton radius puzzle, *Eur. Phys. J. A* 52 (11) (2016) 331, doi:10.1140/epja/i2016-16331-7, 1609.06722.
- [48] William R. Frazer, Jose R. Fulco, Effect of a pion pion scattering resonance on nucleon structure, *Phys. Rev. Lett.* 2 (1959) 365, doi:10.1103/PhysRevLett.2.365.
- [49] G. Höhler, Pion-Nukleon-Streuung: Methoden und Ergebnisse, in: H. Schopper (Ed.), *Landolt-Börnstein*, 9b2, Springer, Berlin 1983.
- [50] G. J. Gounaris, J. J. Sakurai, Finite width corrections to the vector meson dominance prediction for $\rho \rightarrow e^+e^-$, *Phys. Rev. Lett.* 21 (1968) 244–247, doi:10.1103/PhysRevLett.21.244.
- [51] V. Bernard, Norbert Kaiser, Ulf-G. Meißner, Nucleon electroweak form-factors: Analysis of their spectral functions, *Nucl. Phys. A* 611 (1996) 429–441, doi:10.1016/S0375-9474(96)00291-6, hep-ph/9607428.
- [52] N. Kaiser, E. Passemar, Spectral functions of nucleon form factors: Three-pion continua at low energies, *Eur. Phys. J. A* 55 (2) (2019) 16, doi:10.1140/epja/i2019-12680-y, 1901.02865.
- [53] H.-W. Hammer, M. J. Ramsey-Musolf, Spectral content of isoscalar nucleon form-factors, *Phys. Rev. C* 60 (1999) 045205, doi:10.1103/PhysRevC.60.045205, [Erratum: *Phys.Rev.C* 62, 049903 (2000)], hep-ph/9812261.
- [54] H.-W. Hammer, M. J. Ramsey-Musolf, K anti-K continuum and isoscalar nucleon form-factors, *Phys. Rev. C* 60 (1999) 045204, doi:10.1103/PhysRevC.60.045204, [Erratum: *Phys.Rev.C* 62, 049902 (2000)], hep-ph/9903367.
- [55] Ulf-G. Meißner, V. Mull, J. Speth, J. W. van Orden, Strange vector currents and the OZI rule, *Phys. Lett. B* 408 (1997) 381–386, doi:10.1016/S0370-2693(97)00828-9, hep-ph/9701296.
- [56] M. A. Belushkin, H.-W. Hammer, U.-G. Meißner, Dispersion analysis of the nucleon form-factors including meson continua, *Phys. Rev. C* 75 (2007) 035202, doi:10.1103/PhysRevC.75.035202, hep-ph/0608337.
- [57] Y. Ünal, Ulf-G. Meißner, Chiral constraints on the isoscalar electromagnetic spectral functions of the nucleon from leading order vector meson couplings, *Phys. Lett. B* 794 (2019) 103–108, doi:10.1016/j.physletb.2019.05.029, 1902.03143.
- [58] William R. Frazer, Jose R. Fulco, Partial-Wave Dispersion Relations for the Process $\pi + \pi \rightarrow N + \bar{N}$, *Phys. Rev.* 117 (1960) 1603–1609, doi:10.1103/PhysRev.117.1603.
- [59] William R. Frazer, Jose R. Fulco, Effect of a Pion-Pion Scattering Resonance on Nucleon Structure. II, *Phys. Rev.* 117 (1960) 1609–1614, doi:10.1103/PhysRev.117.1609.

- [60] S. Ciulli, C. Pomponiu, I. Sabba Stefanescu, Analytic Extrapolation Techniques and Stability Problems in Dispersion Relation Theory, *Acta Phys. Austriaca Suppl.* 14 (1975) 469–470, doi:10.1007/978-3-7091-8424-0_8.
- [61] I. Sabba Stefanescu, On the Stable Analytic Continuation With Rational Functions, *J. Math. Phys.* 21 (1980) 175, doi:10.1063/1.524317.
- [62] S. Kopecky, P. Riehs, J. A. Harvey, N. W. Hill, New Measurement of the Charge Radius of the Neutron, *Phys. Rev. Lett.* 74 (1995) 2427–2430, doi:10.1103/PhysRevLett.74.2427.
- [63] S. Kopecky, M. Krenn, P. Riehs, S. Steiner, John A. Harvey, N. W. Hill, M. Pernicka, Neutron charge radius determined from the energy dependence of the neutron transmission of liquid Pb-208 and Bi-209, *Phys. Rev. C* 56 (1997) 2229–2237, doi:10.1103/PhysRevC.56.2229.
- [64] A. A. Filin, V. Baru, E. Epelbaum, H. Krebs, D. Möller, P. Reinert, Extraction of the neutron charge radius from a precision calculation of the deuteron structure radius, *Phys. Rev. Lett.* 124 (8) (2020) 082501, doi:10.1103/PhysRevLett.124.082501, 1911.04877.
- [65] A. A. Filin, D. Möller, V. Baru, E. Epelbaum, H. Krebs, P. Reinert, High-accuracy calculation of the deuteron charge and quadrupole form factors in chiral effective field theory, *Phys. Rev. C* 103 (2) (2021) 024313, doi:10.1103/PhysRevC.103.024313, 2009.08911.
- [66] G. Peter Lepage, Stanley J. Brodsky, Exclusive Processes in Perturbative Quantum Chromodynamics, *Phys. Rev. D* 22 (1980) 2157, doi:10.1103/PhysRevD.22.2157.
- [67] Andrea Bianconi, Egle Tomasi-Gustafsson, Periodic interference structures in the timelike proton form factor, *Phys. Rev. Lett.* 114 (23) (2015) 232301, doi:10.1103/PhysRevLett.114.232301, 1503.02140.
- [68] J. P. Lees, et al. (BaBar), Study of $e^+e^- \rightarrow p\bar{p}$ via initial-state radiation at BABAR, *Phys. Rev. D* 87 (9) (2013) 092005, doi:10.1103/PhysRevD.87.092005, 1302.0055.
- [69] G. Höhler, E. Pietarinen, I. Sabba Stefanescu, F. Borkowski, G. G. Simon, V. H. Walther, R. D. Wendling, Analysis of Electromagnetic Nucleon Form-Factors, *Nucl. Phys. B* 114 (1976) 505–534, doi:10.1016/0550-3213(76)90449-1.
- [70] P. Mergell, Ulf-G. Meißner, D. Drechsel, Dispersion theoretical analysis of the nucleon electromagnetic form-factors, *Nucl. Phys. A* 596 (1996) 367–396, doi:10.1016/0375-9474(95)00339-8, hep-ph/9506375.
- [71] H.-W. Hammer, Nucleon form-factors in dispersion theory, *Eur. Phys. J. A* 28 (2006) 49–57, doi:10.1140/epja/i2006-09-006-5, hep-ph/0602121.
- [72] F. James, M. Roos, Minuit: A System for Function Minimization and Analysis of the Parameter Errors and Correlations, *Comput. Phys. Commun.* 10 (1975) 343–367, doi:10.1016/0010-4655(75)90039-9.
- [73] B. Efron, R. Tibshirani, An introduction to the bootstrap, *Statist. Sci.* 57 (1) (1986) 54–75.
- [74] Matthias R. Schindler, Daniel R. Phillips, Bayesian Methods for Parameter Estimation in Effective Field Theories, *Annals Phys.* 324 (2009) 682–708, doi:10.1016/j.aop.2008.09.003, [Erratum: *Annals Phys.* 324, 2051–2055 (2009)], 0808.3643.
- [75] S. Wesolowski, N. Klco, R. J. Furnstahl, D. R. Phillips, A. Thapaliya, Bayesian parameter estimation for effective field theories, *J. Phys. G* 43 (7) (2016) 074001, doi:10.1088/0954-3899/43/7/074001, 1511.03618.
- [76] Yong-Hui Lin, Hans-Werner Hammer, Ulf-G Meißner, High-precision determination of the electric and magnetic radius of the proton, *Phys. Lett. B* 816 (2021) 136254, doi:10.1016/j.physletb.2021.136254, 2102.11642.
- [77] W. Xiong, et al., A small proton charge radius from an electron–proton scattering experiment, *Nature* 575 (7781) (2019) 147–150, doi:10.1038/s41586-019-1721-2.
- [78] J. C. Bernauer, et al. (A1), Electric and magnetic form factors of the proton, *Phys. Rev. C* 90 (1) (2014) 015206, doi:10.1103/PhysRevC.90.015206, 1307.6227.
- [79] V. Punjabi, et al., Proton elastic form-factor ratios to $Q^{*2} = 3.5\text{-GeV}^{*2}$ by polarization transfer, *Phys. Rev. C* 71 (2005) 055202, doi:10.1103/PhysRevC.71.055202, [Erratum: *Phys. Rev. C* 71, 069902 (2005)], nucl-ex/0501018.
- [80] A. J. R. Puckett, et al., Recoil Polarization Measurements of the Proton Electromagnetic Form Factor Ratio to $Q^2 = 8.5\text{ GeV}^2$, *Phys. Rev. Lett.* 104 (2010) 242301, doi:10.1103/PhysRevLett.104.242301, 1005.3419.
- [81] M. Mezziane, et al. (GEP2gamma), Search for effects beyond the Born approximation in polarization transfer observables in ep elastic scattering, *Phys. Rev. Lett.* 106 (2011) 132501, doi:10.1103/PhysRevLett.106.132501, 1012.0339.
- [82] A. J. R. Puckett, et al., Final Analysis of Proton Form Factor Ratio Data at $Q^2 = 4.0, 4.8$ and 5.6 GeV^2 , *Phys. Rev. C* 85 (2012) 045203, doi:10.1103/PhysRevC.85.045203, 1102.5737.
- [83] S. Riordan, et al., Measurements of the Electric Form Factor of the Neutron up to $Q^2 = 3.4\text{ GeV}^2$ using the Reaction ${}^3\bar{H}e(\vec{e}, e'n)pp$, *Phys. Rev. Lett.* 105 (2010) 262302, doi:10.1103/PhysRevLett.105.262302, 1008.1738.
- [84] Medina Ablikim, et al. (BESIII), Measurement of proton electromagnetic form factors in the time-like region using initial state radiation at BESIII, *Phys. Lett. B* 817 (2021) 136328, doi:10.1016/j.physletb.2021.136328, 2102.10337.
- [85] Medina Ablikim, et al. (BESIII), Measurement of proton electromagnetic form factors in $e^+e^- \rightarrow p\bar{p}$ in the energy region 2.00 - 3.08 GeV, *Phys. Rev. Lett.* 124 (4) (2020) 042001, doi:10.1103/PhysRevLett.124.042001, 1905.09001.
- [86] M. Ablikim, et al. (BESIII), Study of the process $e^+e^- \rightarrow p\bar{p}$ via initial state radiation at BESIII, *Phys. Rev. D* 99 (9) (2019) 092002, doi:10.1103/PhysRevD.99.092002, 1902.00665.
- [87] M. Ablikim, et al. (BESIII), Measurement of the proton form factor by studying $e^+e^- \rightarrow p\bar{p}$, *Phys. Rev. D* 91 (11) (2015) 112004, doi:10.1103/PhysRevD.91.112004, 1504.02680.
- [88] M. Ambrogiani, et al. (E835), Measurements of the magnetic form-factor of the proton in the timelike region at large momentum transfer, *Phys. Rev. D* 60 (1999) 032002, doi:10.1103/PhysRevD.60.032002.
- [89] M. Andreotti, et al., Measurements of the magnetic form-factor of the proton for timelike momentum transfers, *Phys. Lett. B* 559 (2003) 20–25, doi:10.1016/S0370-2693(03)00300-9.
- [90] Medina Ablikim, et al. (BESIII), Oscillating features in the electromagnetic structure of the neutron, *Nature Phys.* 17 (11) (2021) 1200–1204, doi:10.1038/s41567-021-01345-6, 2103.12486.
- [91] V. P. Druzhinin, S. I. Serednyakov, Measurement of the $e^+e^- \rightarrow n\bar{n}$ cross section with the SND detector at the VEPP-2000 collider, *EPJ Web Conf.* 212 (2019) 07007, doi:10.1051/epjconf/201921207007.
- [92] John Arrington, Kees de Jager, Charles F. Perdrisat, Nucleon Form Factors: A Jefferson Lab Perspective, *J. Phys. Conf. Ser.* 299 (2011) 012002, doi:10.1088/1742-6596/299/1/012002, 1102.2463.
- [93] H.-W. Hammer, D. Drechsel, Ulf-G. Meißner, On the pion cloud of the nucleon, *Phys. Lett. B* 586 (2004) 291–296, doi:10.1016/j.physletb.2003.12.073, hep-ph/0310240.
- [94] Ulf-G. Meißner, The Pion cloud of the nucleon: Facts and popular fantasies, *AIP Conf. Proc.* 904 (1) (2007) 142–150, doi:10.1063/1.2734299, nucl-th/0701094.
- [95] Randolf Pohl, Ronald Gilman, Gerald A. Miller, Krzysztof Pachucki, Muonic hydrogen and the proton radius puzzle, *Ann. Rev. Nucl. Part. Sci.* 63 (2013) 175–204, doi:10.1146/annurev-nucl-102212-170627, 1301.0905.
- [96] Jean-Philippe Karr, Dominique Marchand, Eric Voutier, The proton size, *Nature Rev. Phys.* 2 (11) (2020) 601–614, doi:10.1038/s42254-020-0229-x.

- [97] Haiyan Gao, Marc Vanderhaeghen, The proton charge radius, *Rev. Mod. Phys.* 94 (1) (2022) 015002, doi:10.1103/RevModPhys.94.015002, 2105.00571.
- [98] Aldo Antognini, et al., Proton Structure from the Measurement of $2S - 2P$ Transition Frequencies of Muonic Hydrogen, *Science* 339 (2013) 417–420, doi:10.1126/science.1230016.
- [99] Peter J. Mohr, Barry N. Taylor, David B. Newell, CODATA Recommended Values of the Fundamental Physical Constants: 2006, *Rev. Mod. Phys.* 80 (2008) 633–730, doi:10.1103/RevModPhys.80.633, 0801.0028.
- [100] <https://physics.nist.gov/cgi-bin/cuu/Value?rp>.
- [101] Peter Mohr, David Newell, Barry Taylor, Eite Tiesinga, CODATA Recommended Values of the Fundamental Physical Constants: 2022 (2024), 2409.03787.
- [102] A. C. Zemach, Proton Structure and the Hyperfine Shift in Hydrogen, *Phys. Rev.* 104 (1956) 1771–1781, doi:10.1103/PhysRev.104.1771.
- [103] J. C. Bernauer, et al. (A1), High-precision determination of the electric and magnetic form factors of the proton, *Phys. Rev. Lett.* 105 (2010) 242001, doi:10.1103/PhysRevLett.105.242001, 1007.5076.
- [104] Dalibor Djukanovic, Georg von Hippel, Harvey B. Meyer, Konstantin Ottnad, Miguel Salg, Hartmut Wittig, Precision Calculation of the Electromagnetic Radii of the Proton and Neutron from Lattice QCD, *Phys. Rev. Lett.* 132 (21) (2024) 211901, doi:10.1103/PhysRevLett.132.211901, 2309.07491.
- [105] Ryutarō Tsuji, Yasumichi Aoki, Ken-Ichi Ishikawa, Yoshinobu Kuramashi, Shoichi Sasaki, Kohei Sato, Eigo Shintani, Hiromasa Watanabe, Takeshi Yamazaki (PACS), Nucleon form factors in $N_f=2+1$ lattice QCD at the physical point: Finite lattice spacing effect on the root-mean-square radii, *Phys. Rev. D* 109 (9) (2024) 094505, doi:10.1103/PhysRevD.109.094505, 2311.10345.
- [106] Yong-Hui Lin, Hans-Werner Hammer, Ulf-G. Meißner, The proton magnetic radius: A new puzzle?, *Sci. Bull.* 69 (2024) 419–421, doi:10.1016/j.scib.2023.12.038, 2312.08694.
- [107] G. Bardin, et al., Determination of the electric and magnetic form-factors of the proton in the timelike region, *Nucl. Phys. B* 411 (1994) 3–32, doi:10.1016/0550-3213(94)90052-3.
- [108] I. T. Lorenz, H.-W. Hammer, U.-G. Meißner, New structures in the proton-antiproton system, *Phys. Rev. D* 92 (3) (2015) 034018, doi:10.1103/PhysRevD.92.034018, 1506.02282.
- [109] Qin-He Yang, Di Guo, Ling-Yun Dai, Johann Haidenbauer, Xian-Wei Kang, Ulf-G. Meißner, New insights into the oscillations of the nucleon electromagnetic form factors, *Sci. Bull.* 68 (2023) 2729–2733, doi:10.1016/j.scib.2023.09.036, 2206.01494.
- [110] Ri-Qing Qian, Zhan-Wei Liu, Xu Cao, Xiang Liu, Toy model to understand the oscillatory behavior in timelike nucleon form factors, *Phys. Rev. D* 107 (9) (2023) L091502, doi:10.1103/PhysRevD.107.L091502, 2211.11555.
- [111] Qin-He Yang, Di Guo, Ming-Yan Li, Ling-Yun Dai, Johann Haidenbauer, Ulf-G. Meißner, Study of the electromagnetic form factors of the nucleons in the timelike region, *JHEP* 08 (2024) 208, doi:10.1007/JHEP08(2024)208, 2404.12448.
- [112] Francesco Rosini, Simone Pacetti, Olga Shekhovtsova, Egle Tomasi-Gustafsson, Microscopic parametrization of the near threshold oscillations of the nucleon time-like effective electromagnetic form factors, *Eur. Phys. J. A* 60 (7) (2024) 144, doi:10.1140/epja/s10050-024-01365-9, 2403.02916.
- [113] Silvan S. Schweber, Hans A. Bethe, Frederic de Hoffmann, *Mesons and fields. Volume 1: Fields*, Peterson and Company, Evanston, Illinois 1955.
- [114] Veronique Bernard, Thomas R. Hemmert, Ulf-G. Meißner, Cutoff schemes in chiral perturbation theory and the quark mass expansion of the nucleon mass, *Nucl. Phys. A* 732 (2004) 149–170, doi:10.1016/j.nuclphysa.2003.12.011, hep-ph/0307115.
- [115] Karin Schönning (BESIII), Hyperon Structure at BESIII, *Acta Phys. Polon. Supp.* 16 (3) (2023) 14, doi:10.5506/APhysPolBSupp.16.3-A14.
- [116] Ling-Yun Dai, Johann Haidenbauer, Ulf-G. Meißner, Electromagnetic form factors of hyperons in the timelike region: A short review (2024), 2412.07543.
- [117] Carlos Granados, Stefan Leupold, Elisabetta Perotti, The electromagnetic Sigma-to-Lambda hyperon transition form factors at low energies, *Eur. Phys. J. A* 53 (6) (2017) 117, doi:10.1140/epja/i2017-12324-4, 1701.09130.
- [118] Yong-Hui Lin, Hans-Werner Hammer, Ulf-G. Meißner, The electromagnetic Sigma-to-Lambda transition form factors with coupled-channel effects in the space-like region, *Eur. Phys. J. A* 59 (3) (2023) 54, doi:10.1140/epja/s10050-023-00973-1, 2205.00850.
- [119] Olov Junker, Stefan Leupold, Elisabetta Perotti, Tímea Vitos, Electromagnetic form factors of the transition from the spin-3/2 Σ to the Λ hyperon, *Phys. Rev. C* 101 (1) (2020) 015206, doi:10.1103/PhysRevC.101.015206, 1910.07396.
- [120] Yong-Hui Lin, Hans-Werner Hammer, Ulf-G. Meißner, Dispersion-theoretical analysis of the electromagnetic form factors of the Λ hyperon, *Eur. Phys. J. C* 82 (12) (2022) 1091, doi:10.1140/epjc/s10052-022-11056-8, 2208.14802.
- [121] E. J. Downie (MUSE), The MUSE experiment, *EPJ Web Conf.* 73 (2014) 07005, doi:10.1051/epjconf/20147307005.
- [122] B. Adams, et al., Letter of Intent: A New QCD facility at the M2 beam line of the CERN SPS (COMPASS++/AMBER) (2018), 1808.00848.